



HAL
open science

The X-CLASS survey: A catalogue of 1646 X-ray-selected galaxy clusters up to $z \sim 1.5$

E. Koulouridis, N. Clerc, T. Sadibekova, M. Chira, E. Drigga, L. Faccioli, J.
Le Fèvre, C. Garrel, E. Gaynullina, A. Gkini, et al.

► **To cite this version:**

E. Koulouridis, N. Clerc, T. Sadibekova, M. Chira, E. Drigga, et al.. The X-CLASS survey: A catalogue of 1646 X-ray-selected galaxy clusters up to $z \sim 1.5$. *Astronomy and Astrophysics - A&A*, 2021, 652, pp.A12. 10.1051/0004-6361/202140566 . hal-03387880

HAL Id: hal-03387880

<https://hal.science/hal-03387880>

Submitted on 21 Oct 2021

HAL is a multi-disciplinary open access archive for the deposit and dissemination of scientific research documents, whether they are published or not. The documents may come from teaching and research institutions in France or abroad, or from public or private research centers.

L'archive ouverte pluridisciplinaire **HAL**, est destinée au dépôt et à la diffusion de documents scientifiques de niveau recherche, publiés ou non, émanant des établissements d'enseignement et de recherche français ou étrangers, des laboratoires publics ou privés.

The X-CLASS survey: A catalogue of 1646 X-ray-selected galaxy clusters up to $z \sim 1.5$ *

E. Koulouridis¹ , N. Clerc², T. Sadibekova³, M. Chira^{1,4}, E. Drigga^{1,4}, L. Faccioli³, J. P. Le Fèvre³, C. Garrel³, E. Gaynullina⁵, A. Gkini^{1,6}, M. Kosiba^{7,8}, F. Pacaud⁹, M. Pierre³, J. Ridl¹⁰, K. Tazhenova³, C. Adami¹¹, B. Altieri¹², J.-C. Baguley¹³, R. Cabanac², E. Cucchetti², A. Khalikova⁵, M. Lieu¹⁴, J.-B. Melin¹⁵, M. Molham¹⁶, M. E. Ramos-Ceja¹⁰, G. Soucail², A. Takey¹⁶, and I. Valtchanov¹⁷

¹ Institute for Astronomy & Astrophysics, Space Applications & Remote Sensing, National Observatory of Athens, 15236 Palaia Penteli, Greece
e-mail: ekoulouridis@noa.gr

² IRAP, Université de Toulouse, CNRS, CNES, UT3, Toulouse, France

³ AIM, CEA, CNRS, Université Paris-Saclay, Université Paris Diderot, Sorbonne Paris Cité, 91191 Gif-sur-Yvette, France

⁴ Department of Physics, Aristotle University of Thessaloniki, Thessaloniki 54124, Greece

⁵ Ulugh Beg Astronomical Institute of Uzbekistan Academy of Sciences, 33 Astronomicheskaya Str., Tashkent 100052, Uzbekistan

⁶ Department of Astrophysics, Astronomy & Mechanics, Faculty of Physics, National and Kapodistrian University of Athens, Panepistimiopolis Zografou, Athens 15784, Greece

⁷ Department of Theoretical Physics and Astrophysics, Faculty of Science, Masaryk University, Kotlářská 2, Brno 611 37, Czech Republic

⁸ Dipartimento di Fisica, Università degli Studi di Torino, Via Pietro Giuria 1, 10125 Torino, Italy

⁹ Argelander-Institut für Astronomie, University of Bonn, Auf dem Hügel 71, 53121 Bonn, Germany

¹⁰ Max-Planck-Institut für Extraterrestrische Physik, Giessenbachstraße 1, 85748 Garching, Germany

¹¹ LAM, OAMP, Université Aix-Marseille, CNRS, Pôle de l'Étoile, Site de Château Gombert, 38 Rue Frédéric Joliot-Curie, 13388 Marseille 13 Cedex, France

¹² European Space Astronomy Centre, ESA, Villanueva de la Cañada 28691, Madrid, Spain

¹³ School of Physics, HH Wills Physics Laboratory, Tyndall Avenue, Bristol BS8 1TL, UK

¹⁴ School of Physics & Astronomy, University of Nottingham, University Park, Nottingham NG7 2RD, UK

¹⁵ IRFU, CEA, Université Paris-Saclay, 91191 Gif-sur-Yvette, France

¹⁶ National Research Institute of Astronomy and Geophysics (NRIAG), 11421 Helwan, Cairo, Egypt

¹⁷ Telespazio UK for ESA, European Space Astronomy Centre, Operations Department, 28691 Villanueva de la Cañada, Spain

Received 15 February 2021 / Accepted 30 April 2021

ABSTRACT

Context. Cosmological probes based on galaxy clusters rely on cluster number counts and large-scale structure information. X-ray cluster surveys are well suited for this purpose because they are far less affected by projection effects than optical surveys, and cluster properties can be predicted with good accuracy.

Aims. The XMM Cluster Archive Super Survey, X-CLASS, is a serendipitous search of X-ray-detected galaxy clusters in 4176 *XMM-Newton* archival observations until August 2015. All observations are clipped to exposure times of 10 and 20 ks to obtain uniformity, and they span ~ 269 deg² across the high-Galactic latitude sky ($|b| > 20^\circ$). The main goal of the survey is the compilation of a well-selected cluster sample suitable for cosmological analyses.

Methods. We describe the detection algorithm, the visual inspection, the verification process, and the redshift validation of the cluster sample, as well as the cluster selection function computed by simulations. We also present the various metadata that are released with the catalogue, along with two different count-rate measurements, an automatic one provided by the pipeline, and a more detailed and accurate interactive measurement. Furthermore, we provide the redshifts of 124 clusters obtained with a dedicated multi-object spectroscopic follow-up programme.

Results. With this publication, we release the new X-CLASS catalogue of 1646 well-selected X-ray-detected clusters over a wide sky area, along with their selection function. The sample spans a wide redshift range, from the local Universe up to $z \sim 1.5$, with 982 spectroscopically confirmed clusters, and over 70 clusters above $z = 0.8$. The redshift distribution peaks at $z \sim 0.1$, while if we remove the pointed observations it peaks at $z \sim 0.3$. Because of its homogeneous selection and thorough verification, the cluster sample can be used for cosmological analyses, but also as a test-bed for the upcoming eROSITA observations and other current and future large-area cluster surveys. It is the first time that such a catalogue is made available to the community via an interactive database which gives access to a wealth of supplementary information, images, and data.

Key words. X-rays: galaxies: clusters – galaxies: clusters: general – surveys – catalogs – large-scale structure of Universe – galaxies: clusters: intracluster medium

* Full Tables 3 and D.1 are also available at the CDS via anonymous ftp to cdsarc.u-strasbg.fr (130.79.128.5) or via <http://cdsarc.u-strasbg.fr/viz-bin/cat/J/A+A/652/A12>

1. Introduction

Observational cosmology has been coming into increasing focus over the last two decades, propelled by wide-area surveys, such as for example the Sloan Digital Sky Survey (SDSS; Blanton et al. 2017) and the Wide-field Infrared Survey Explorer (WISE; Wright et al. 2010), but also by modern observatories like eROSITA (Merloni et al. 2012; Predehl et al. 2021) and *Euclid* (Laureijs et al. 2011). All these surveys gain additional value from supplemental multi-wavelength observations, with a growing synergy between space- and ground-based observatories. Wide-area surveys constitute an essential asset for large-scale structure studies because they can provide a unique handle on the abundance of massive objects, a crucial element for cosmology. Nevertheless, the collection, analysis, and treatment of the data, in order to create valuable user-friendly catalogues and archives for the scientific community, is increasingly challenging and time-consuming, despite the availability of modern tools and computational capabilities. Therefore, such endeavours are rightfully dubbed ‘legacy surveys’.

In this framework, cosmologists seek large samples of galaxy clusters, spanning a wide range of masses and redshifts, in order to use them as cosmological probes. These probes mainly rely on cluster number counts and large-scale structure information to capture the evolution of the halo mass function and the halo spatial distribution across cosmic times. Galaxy clusters are the most massive gravitationally bound structures in the Universe. They are mainly dominated by dark matter (~85% of the total mass), while the hot X-ray-emitting intracluster medium (ICM) accounts for most of their baryonic mass (e.g. Plionis et al. 2008). Therefore, galaxy clusters can be identified in various wavelengths (e.g. Vikhlinin et al. 2009; Mantz et al. 2010; Rozo et al. 2010; Sehgal et al. 2011; Benson et al. 2013; Planck Collaboration XX 2014), and X-ray surveys in particular have proven very effective in detecting large numbers of them (e.g. Fassbender et al. 2011; Willis et al. 2013; Pierre et al. 2004, 2016; Takey et al. 2016; Adami et al. 2018) including many at redshifts $z > 1$, with the most distant clusters found up to a redshift of $z \sim 2$ (Santos et al. 2011; Mantz et al. 2018).

The X-ray selection, although possibly biased towards baryon-rich and relaxed clusters (e.g. Andreon et al. 2016; O’Sullivan et al. 2017), presents two main advantages: First, the cluster properties can be self-consistent and easily predicted by *ab initio* models, because the measurable X-ray parameters are closely related to the mass of the cluster (e.g. Frenk et al. 1990; van Haarlem et al. 1997). Second, cluster catalogues are hardly affected by projection effects (e.g. Ramos-Ceja et al. 2019), namely the inclusion of spurious sources resulting from the projection of unrelated systems along the line of sight, because the centrally concentrated X-ray emission clearly indicates the presence of gas trapped in the potential well of a cluster (e.g. Frenk et al. 1990; Reblinsky & Bartelmann 1999).

Consequently, X-ray surveys have had a key role in the systematic search for galaxy clusters, initially with the historical HEAO-1 X-ray observatory (Piccinotti et al. 1982) and then with the Einstein observatory Medium Sensitivity Survey (Gioia et al. 1990; Henry et al. 1992). Many other important surveys have been conducted over the course of the last three decades, starting with the ROSAT observatory, which provided the instrumentation for REFLEX-I, II (Böhringer et al. 2001, 2014), NORAS (Böhringer et al. 2000), MACS (Ebeling et al. 2001), ROSAT-NEP (Henry et al. 2006) and CODEX (Finoguenov et al. 2020; Kirkpatrick et al. 2021), and then by *XMM-Newton* and *Chandra* observatories, which allowed COSMOS (Scoville et al.

2007; Finoguenov et al. 2007), XMM-LSS (Pierre et al. 2007; Clerc et al. 2014), XMM-BCS (Šuhada et al. 2012), XCS (Romer et al. 2001; Mehrrens et al. 2012), 2XMMi/SDSS (Takey et al. 2011, 2013, 2014), X-CLASS (Clerc et al. 2012, hereafter CS12), XDCP (Fassbender et al. 2011), and XMM-XXL (Pierre et al. 2016; Adami et al. 2018).

In this context, here we present the new X-CLASS catalogue of 1646 X-ray selected clusters followed by a public release. The catalogue is based on all 9333 XMM archival observations publicly available until August 2015. All observations were filtered following identical criteria to those in CS12: galactic latitudes above 20 deg and not located within the Magellanic Clouds and M31 areas, on sky exposure time larger than 5 ks in each of the three European Photon Imaging Camera (EPIC) detectors, and all three instruments in Imaging mode. This led to the selection of 4176 XMM pointings that went through an identical processing. In Sect. 2 we present the data processing, the resulting sample of galaxy cluster candidates, and their selection function. In Sects. 3 and 4 we describe the various steps of the screening of the candidates and further analysis of the sample. Finally, in Sect. 5 we describe the public database and in Sect. 6 we discuss the results and compare with other cluster catalogues. The full procedure is also illustrated in Fig. 1 in a flowchart. Throughout this paper, we use $H_0 = 70 \text{ km s}^{-1} \text{ Mpc}^{-1}$, $\Omega_m = 0.3$, and $\Omega_\Lambda = 0.7$.

2. Data processing and source detection

The data processing follows the lines of CS12 with improvements and modifications. We recall here the main steps involved and highlight the main changes. Basic parameters used during the various data processing steps can be found in Table 1.

The XMM observations were reduced with the latest calibration files available (August 2015) and light curves were created in the high-energy band to monitor the flaring time-intervals. An automated algorithm identified excess variance in the count-rate time histogram in order to determine acceptable count-rate levels which were later included in the GTIs (good time intervals). More specifically, event lists were filtered from proton and solar flares by creating the high-energy event light curves in the [12–14] keV band for MOS and the [10–12] keV band for PN, and flagging out periods of high event rates (rates greater than 3σ above the mean observation count rate). Event histograms and the corresponding light curves and cut limits are stored in the online database and are available for all pointings. While the above automated procedure is efficient in removing short periods of high flares, it may fail in observations with a high mean particle background. Therefore, although no systematic human verification is performed at this point, parameters and figures were stored in a database and the overall quality of each observation was subsequently inspected by eye during the screening procedure described in Sect. 3.3.

The 4176 observations were homogenised by selecting intervals not contaminated by flares, such that their exposure time in each of the EPIC detectors amounts exactly to 10 ks or 20 ks. This ensures uniformity, enabling the calculation of selection functions. In what follows we refer to XMM observations associated to one of the above two versions as ‘pointings’. Therefore, each original XMM observation may deliver zero, one (10 ks), or two (10 ks and 20 ks) X-CLASS pointings. This resulted in a total of 2461 observations with a 10 ks exposure, of which 1309 also had a 20 ks version. The distribution of these pointings on the sky is shown in Fig. 2. A circular area of radius 13’ around each pointing centre defines the geometric area of a pointing

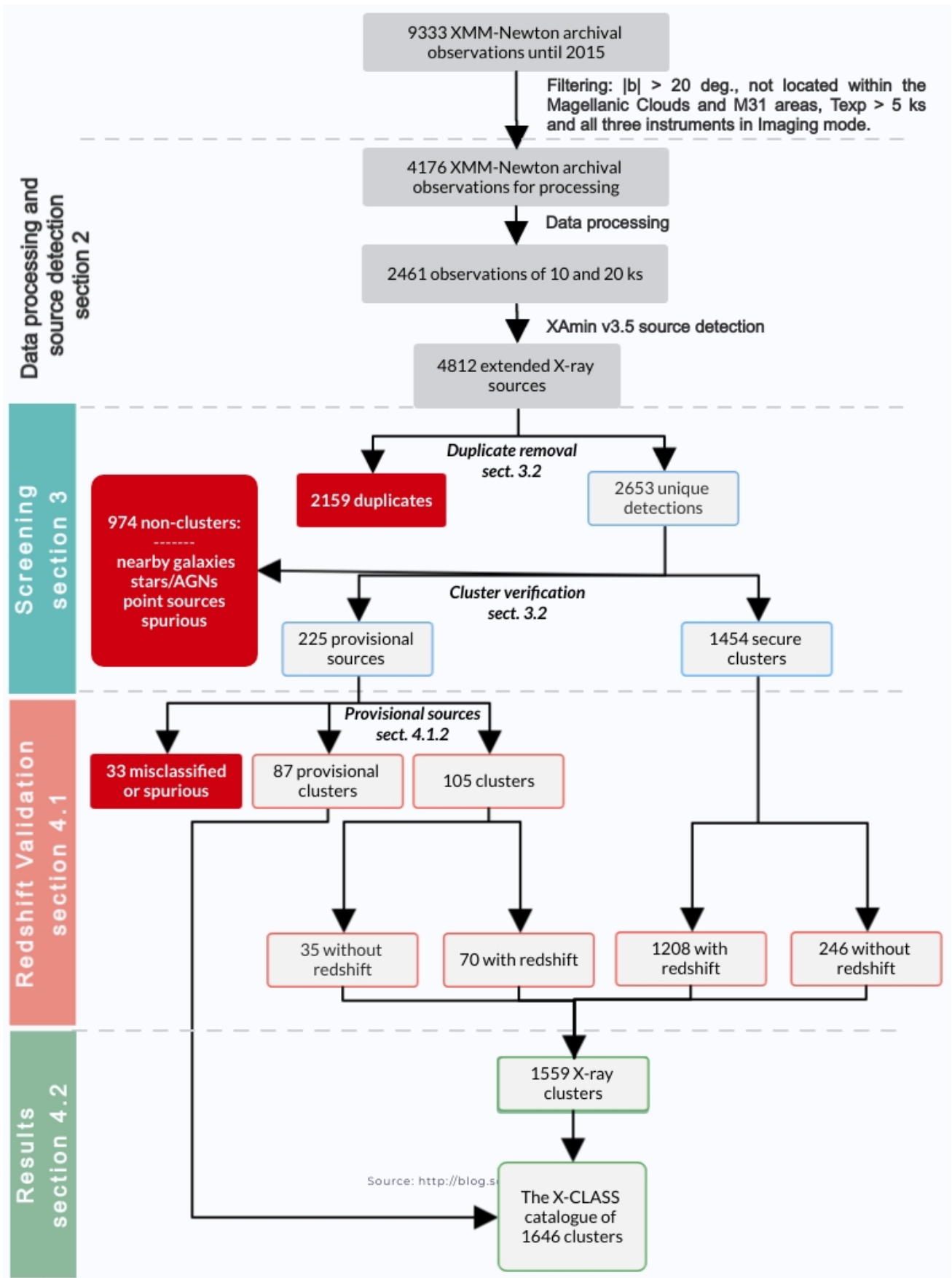


Fig. 1. Flowchart of the overall procedure for the compilation of the new X-CLASS cluster catalogue. Red filled frames contain the sources that were discarded.

Table 1. Data processing parameters.

Parameter	value
<i>Event selection:</i>	
MOS event flag selection	#XMMEA_EM
PN event flag selection	(FLAG & 0x2fb002c)==0
MOS patterns	[0:12]
PN patterns	[0:4]
<i>Image:</i>	
Type	Sky
Configuration	Co-addition of EPIC detectors
Pixel size	2.5 arcsec
Filtering	Wavelet transform (8 scales)
<i>SExtractor:</i>	
Background cell side	64 pixel
Background median filtering	4 cells
Detection threshold	6σ
Detection minimum area	12 pixel
Deblending sub thresholds	64
Deblend min. contrast	0.003

on the sky; sources are detected within this off-axis range only, thereby avoiding strongly vignettted areas on the detectors. The total survey geometrical area is computed by means of two-dimensional Monte-Carlo integration, accounting for the overlaps between pointings, and amounts to 269 deg^2 . We note that pointed observations of clusters have been included in our observation list. Finally, they were processed twice with XAmin v3.5 pipeline (Faccioli et al. 2018) for both exposure times.

Source detection is a three-step process. During the first pass, images in the soft X-ray band, [0.5–2] keV, are created and filtered with a wavelet algorithm, as described in Starck & Pierre (1998). According to that paper, this is the best filtering method for X-ray images that contain few photons and Poisson noise. Most importantly, it was demonstrated that this method is very effective in detecting low-flux extended X-ray sources, which is crucial for our short-exposure time survey. An example of such a filtered observation is presented in Fig. 3.

During a second step, SExtractor (Bertin & Arnouts 1996) was used for source detection. It provided a centroid estimate, the extent of the X-ray emission, and a rough measurement of brightness. The background level is iteratively estimated in image cells by 3σ clipping and a full-resolution background map is constructed by bicubic-spline interpolation. Finally, these parameters served as input for a maximum likelihood fitting routine that applied several source models on the photon image in the soft X-ray band: in particular, a precise point-spread function (PSF) model and an extended β -model (Cavaliere & Fusco-Femiano 1978) described by

$$S_X(r) \propto \left[1 + \left(\frac{r}{\text{EXT}} \right)^2 \right]^{-3\beta+1/2},$$

where EXT is the core radius in arc-seconds and $\beta = 2/3$. For either a point-like or an extended source, the MEDIUM PSF model from the XMM calibration data is used. The SExtractor pixel segmentation mask was used to flag out pixels belonging to neighbouring sources included in the box. In contrast to previous XAmin versions, XAmin v3.5 fixed the position of the extended source fit at the value found by SExtractor. This selection yields 4812 extended X-ray sources.

Only sources classified as ‘‘C1’’ in a pointing were used to build the catalogue. These are characterised by a value of their extended-detection likelihood greater than 32, an extent likelihood greater than 33, and an extent (best-fit core-radius) larger than 5’’ (for more details on these quantities see Faccioli et al. 2018). Simulations of XMM ‘empty’ cosmological fields demonstrated that such thresholds ensure pure samples of extended sources with a controllable selection function (Pacaud et al. 2006). However, XMM-Newton is generally not pointing towards empty fields. The diversity of sources and instrumental artefacts encountered in the archive makes the X-CLASS C1 sample more prone to contamination by non-cluster sources and this is the purpose of the visual inspection process to eliminate those spurious sources (see Sect. 3.3). At this stage, a given C1 detection may appear several times in the source list. This is either due to overlaps between XMM observations, because it appears in both exposure-time versions of the same pointing, or because it has been separated in multiple components, usually by sharp (small-scale) exposure variations due to one (or more) CCD gaps that caused the detection pipeline to segment the detection of extended sources into multiple areas. In the following sections, we describe the cluster selection function and the decontaminating procedure for the removal of duplicate and false detections. We note that clusters detected on observations with missing detectors were discarded from our list, but can be found in Table B.1.

Owing to the uniform exposure time, simulations allow us to accurately determine the selection function of the X-CLASS cluster sample. However, a large number of extended X-ray detections can be due to various other sources, such as for example nearby galaxies, stars, active galactic nuclei (AGNs), double point-sources, and so on. Most of these sources are not modelled in the simulations and should be discarded before reaching a clean cluster sample. We describe this interactive procedure in the following section.

3. Screening of the X-ray cluster candidates

3.1. Previous versions of the catalogue

Our previous analysis of the XMM archive provided a catalogue of 845 sources identified as galaxy clusters among 1514 C1 unique detections on which we performed visual screening. This first catalogue was publicly released in CS12. Sadibekova et al. (2014) cross-matched the redMaPPer optical cluster catalogue (Rykoff et al. 2014) in the northern hemisphere (SDSS photometry) and a subset of the X-CLASS C1 sources. These sources were included as targets of the SPIDERS (SPectroscopic IDentification of ERosita Sources) follow-up programme (Clerc et al. 2016) in SDSS-IV (Blanton et al. 2017) and are further described in Sect. 4.1.3. In addition, a large follow-up programme with the GROND instrument on the MPG/2.2m telescope at La Silla (Greiner et al. 2008) measured 232 photometric redshifts of X-CLASS clusters using 4-band images and is described in Ridl et al. (2017). All 845 clusters of the first data release are included in the current new X-CLASS catalogue.

3.2. Duplicate removal

The initial list of C1 pipeline-detected sources requires a first-pass inspection in order to remove duplicate entries of single sources. An iterative procedure is performed, coupling automatic and manual associations of multiple detections. Starting from the list of 4812 C1 detections, we grouped sources with

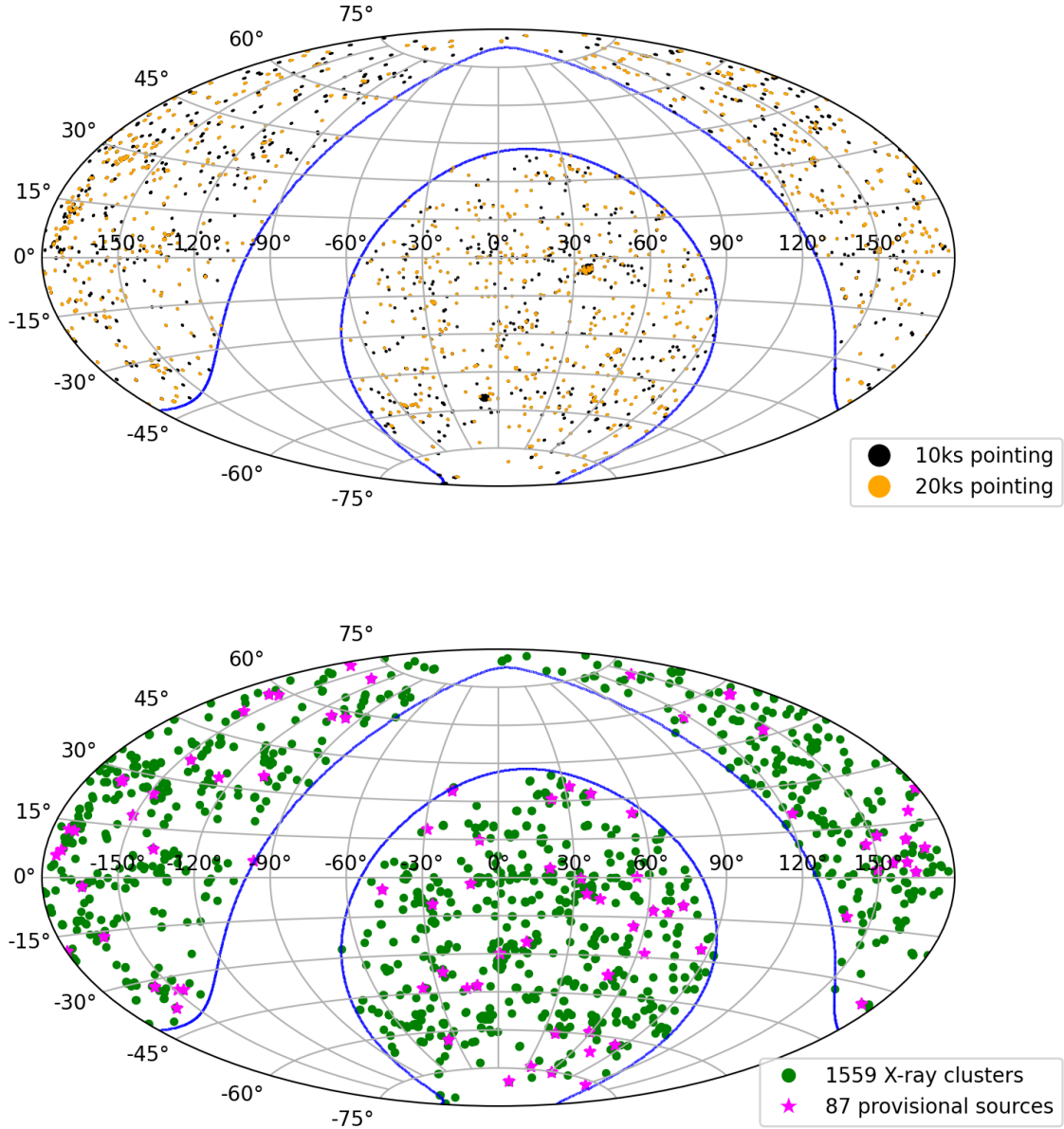


Fig. 2. X-CLASS survey covering a total area of 269.0 deg^2 by 4176 *XMM-Newton* archival observations. *Top panel:* there are 2461 “10 ks” pointings, of which 1309 also have a “20 ks” version. This map in equatorial coordinates shows their location on the sky. The blue line marks the limit of ± 20 deg around the galactic plane. *Bottom panel:* the 1646 X-ray selected galaxy clusters of the X-CLASS catalogue.

a fixed $10''$ distance criterion, reminiscent of the *XMM-Newton* PSF extent. We then ensured that the association flags are correctly set, reflecting the nature of the duplicate (e.g. overlapping pointing, secondary exposure, etc.). Only one entry is selected as the main detection according to the following rules: it needs to be detected on the higher exposure pointing (20 ks if present) and in case of conflict, to have the higher value of extent likelihood. This procedure was repeated within $20''$, $30''$, $40''$, and $60''$ correlation radii. Correlations within the larger two radii were supervised and visually validated in order to prevent false associations. During this step, 2159 sources were identified as duplicate detections, leaving 2653 for further visual inspection.

3.3. Cluster verification

Once the duplication check had been applied, all C1 candidates were interactively screened by expert researchers to identify

non-clusters, spurious detections, or duplicates missed by the algorithm. To this end, we used overlays of X-ray contours on the Digitized Sky Survey (DSS) images using the dedicated database tool. The purpose of this procedure is twofold: (1) remove nearby galaxies, saturated point-sources, X-ray artefacts, and possible unresolved double-sources that also appear as extended sources, and (2) provide an approximate distance indicator depending on the existence of a conspicuous optical counterpart to the X-ray emission, namely: NEARBY ($z < 0.3\text{--}0.4$) and DISTANT ($z > 0.3\text{--}0.4$), where $z \sim 0.3\text{--}0.4$ corresponds to the POSS-II plate limit for typical cluster red-sequence galaxies. Other classifications also included ‘nearby galaxy’ and ‘fossil group’. The procedure involved several researchers from the X-CLASS Collaboration specialised in cluster science and astronomical observations. Each source was inspected by two or more of the researchers who independently decided on its classification. The final classification, based on these decisions, was then

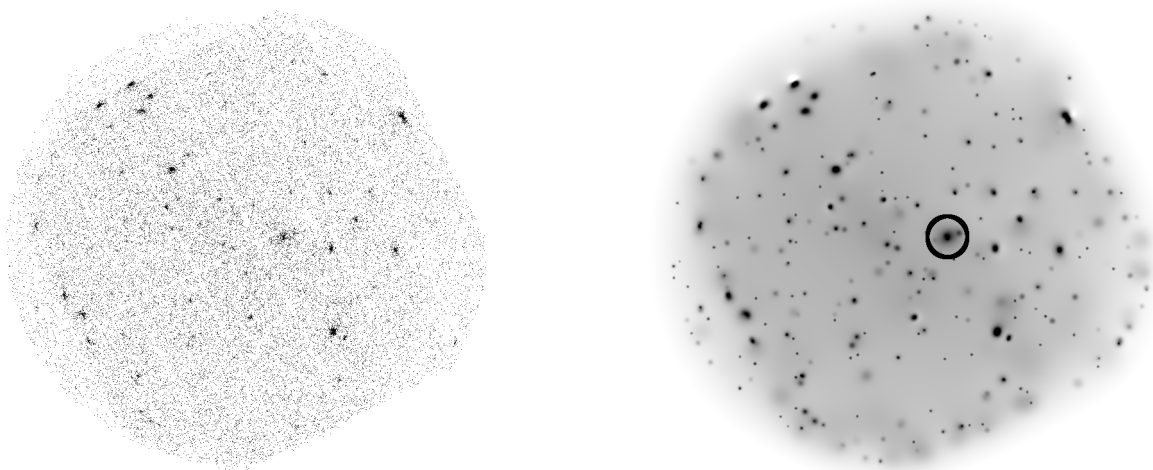


Fig. 3. X-ray image in the [0.5–2] keV X-ray band of a 10 ks *XMM-Newton* observation (*left panel*, mosaic of all three *XMM-Newton* detectors) and the corresponding wavelet filtered image (*right panel*). The images are not background-subtracted and their diameter is 26'. The circle marks the position of a detected cluster candidate. Similar images are available for all X-CLASS clusters in the public database.

assigned to the sources by two expert moderators, who did not participate in the classification. If the classifications provided by the researchers were discrepant, the decision was arbitrated by the moderators. During this step, 974 detections were discarded. All available redshifts were retrieved for the remaining 1679 cluster candidates using the NED extragalactic database and dedicated follow-up observations.

Out of the 1679 sources, 225 were flagged as ‘provisional’, signifying that the nature of the detected source was dubious, and further investigation was needed. The nature of these sources was thoroughly scrutinised at a later time using deeper optical surveys and more current spectroscopic and photometric data not available during the initial catalogue compilation. Their screening is presented in more detail in Sect. 4.1.2.

4. The X-CLASS cluster catalogue

4.1. Redshift validation

4.1.1. Visual inspection

Before the compilation of the X-CLASS public catalogue of galaxy clusters, which we present below, we undertook a thorough inspection of all sources considering the availability of wide and recent optical photometric and spectroscopic surveys. We most frequently used DECaLS (Dey et al. 2019), PanSTARRS (Flewelling et al. 2020), and SDSS-DR16 (Blanton et al. 2017), which provided deeper optical images than those of DSS used in our first pass, and a plethora of spectroscopic data. Our procedure included: combined visual inspection of the X-ray and optical images, matching of our candidates with previously released X-ray or optical catalogues of galaxy clusters, collecting all available spectroscopic data to confirm the redshift of the cluster, and producing all relevant meta-data for inclusion in the database.

More specifically, our first action was to search for previously detected galaxy clusters that coincide with our X-ray detection. This information was mostly readily available from our previous matching, but nevertheless we used the NED database for our sources and have included all recent information. All relevant data are stored in the database and are available to the public. When available, the cross-matching provided a first estimation of the cluster redshift. Then, especially in the

case where no matching cluster was found in the literature, we had to visually inspect the optical and the X-ray image of each cluster candidate. Our first choice for the optical band was PanSTARRS-DR1 colour images (from g and z bands) where we found that a concentration of red cluster galaxies is visible up to a redshift of $z \sim 1$ (see Fig. 4). PanSTARRS is available for the full northern sky and down to a declination of -30° . For a much more limited sky area, DECaLS survey was also available, which is essential for high-redshift cluster candidates. For the rest of the clusters with no deep optical data, we used the DSS images, as we had previously done during our first pass.

Then, for each cluster with an initial estimation for its redshift, we computed the projected 500 kpc radius. We selected this limiting radius as it roughly corresponds to an average R_{500} radius for a moderately rich cluster, and we expect to locate the vast majority of cluster galaxies within this range. The same radius was used for the XXL survey cluster sample (Adami et al. 2018). We then collected data from NED and, when available, from SDSS-DR16, because recent spectroscopic data from the latest release were not yet available in NED. To validate the redshift of an X-ray cluster we chose to implement the same guidelines as for the XXL survey catalogue (Adami et al. 2018). Therefore, the redshift of a cluster can be categorised as follows:

- *Confirmed*: if three or more galaxies with concordant spectroscopic redshifts are found within the 500 kpc radius from the centre of the X-ray detection, or alternatively, if the spectrum of the brightest cluster galaxy (BCG) is available.
- *Tentative*: if one or two galaxies with concordant spectroscopic redshifts are found within the 500 kpc radius.
- *Photometric*: if only photometric redshift information is available in the literature or from our previous dedicated follow-up (Ridl et al. 2017).
- *Provisional*: for cases where the available information does not allow us to verify the existence of a galaxy cluster in this position. Further follow-up observations are needed to safely classify these sources. Although these sources are part of the X-CLASS catalogue, they are not included in the online database, but can be found in Appendix D.

All cluster candidates were reviewed by at least two researchers. However, visual inspection and redshift confirmation was especially critical for the 225 sources previously classified as

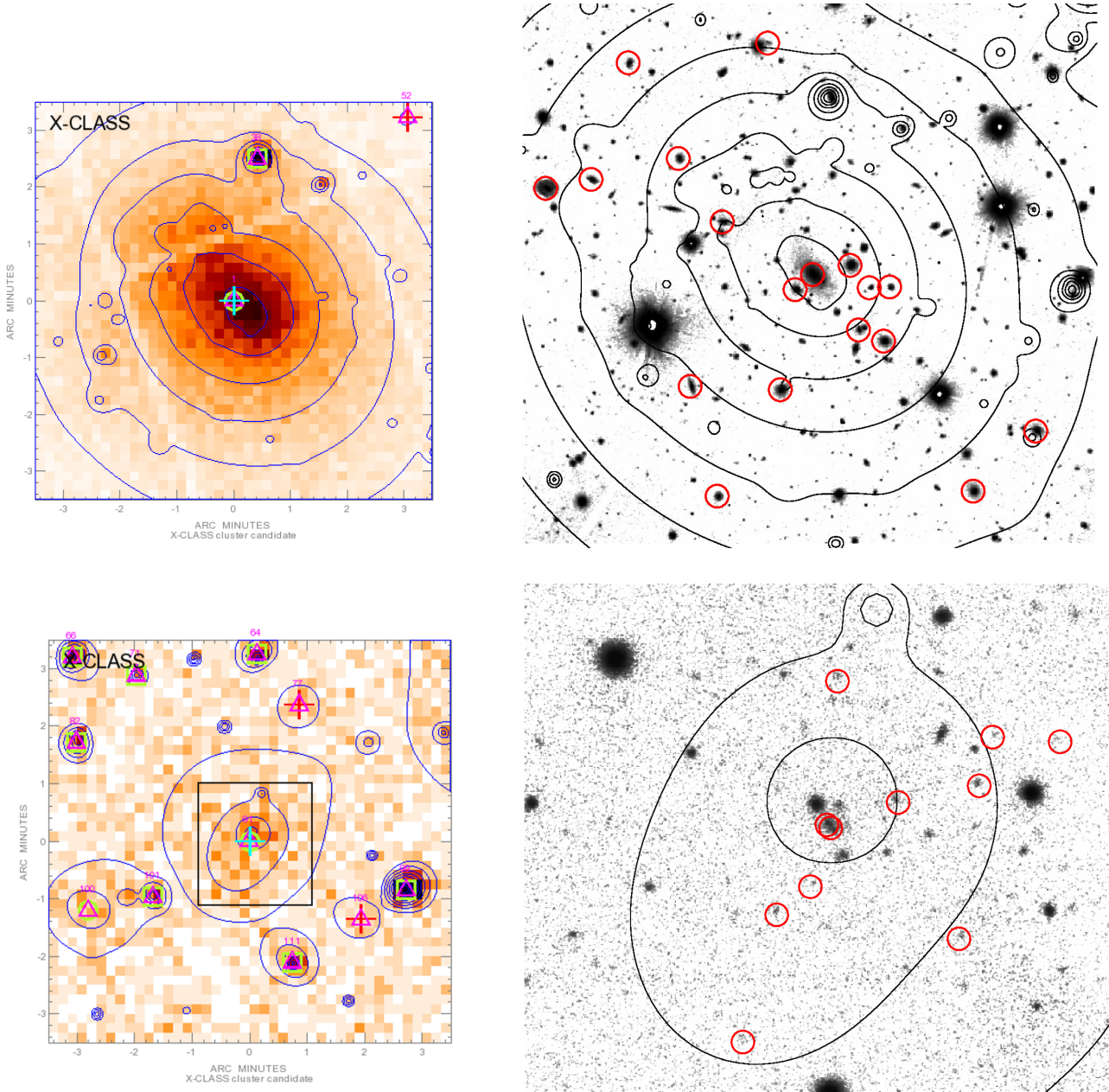


Fig. 4. Examples of X-ray-selected galaxy clusters in the X-CLASS survey. *Top panels:* cluster Xclass0561 (ABELL 2050) at $z = 0.119$ as confirmed by 19 member galaxies. *Bottom panels:* cluster Xclass0219 at $z = 0.791$ as confirmed by 11 member galaxies. *Left panels:* X-ray images and contours. Green circles (squares) mark detections of extended (point-like) sources as classified by the XAmin pipeline. Straight lines that cross the image are CCD gaps of the *XMM-Newton* detector. *Right panels:* *i*-band optical images from PanSTARRS over-plotted with X-ray contours. Red circles mark the member galaxies with available spectroscopic redshift. In the case of Xclass0561, both X-ray and optical images cover the same sky area, while in the case of Xclass0219 the optical image corresponds to the central region of the X-ray image marked with the black square.

‘provisional’, for which we followed the more thorough procedure described in the following section.

4.1.2. Provisional sources

As provisional cases were more challenging for the reviewers, each source was further inspected by two more consortium members. Their task was to simply classify the detection as a true or false cluster, considering all available optical and X-ray data. Out of the 225 sources, 70 were already validated as true clusters (49 confirmed, 12 tentative, and 9 photometric) and were

used to test the reliability of the reviewers. For this step, we considered the classifications of seven researchers (different from those of the previous section), while we discarded those of the two researchers that gave the greatest number of false answers with respect to the already validated sources.

Finally, we require full agreement between the researchers in order to characterise a source as a true cluster, or a spurious or misclassified detection, while sources with discrepant classifications kept their ‘provisional’ status. More precisely, 33 provisional sources were classified as ‘inexistent’ and were discarded from the catalogue, while 35 were identified as true

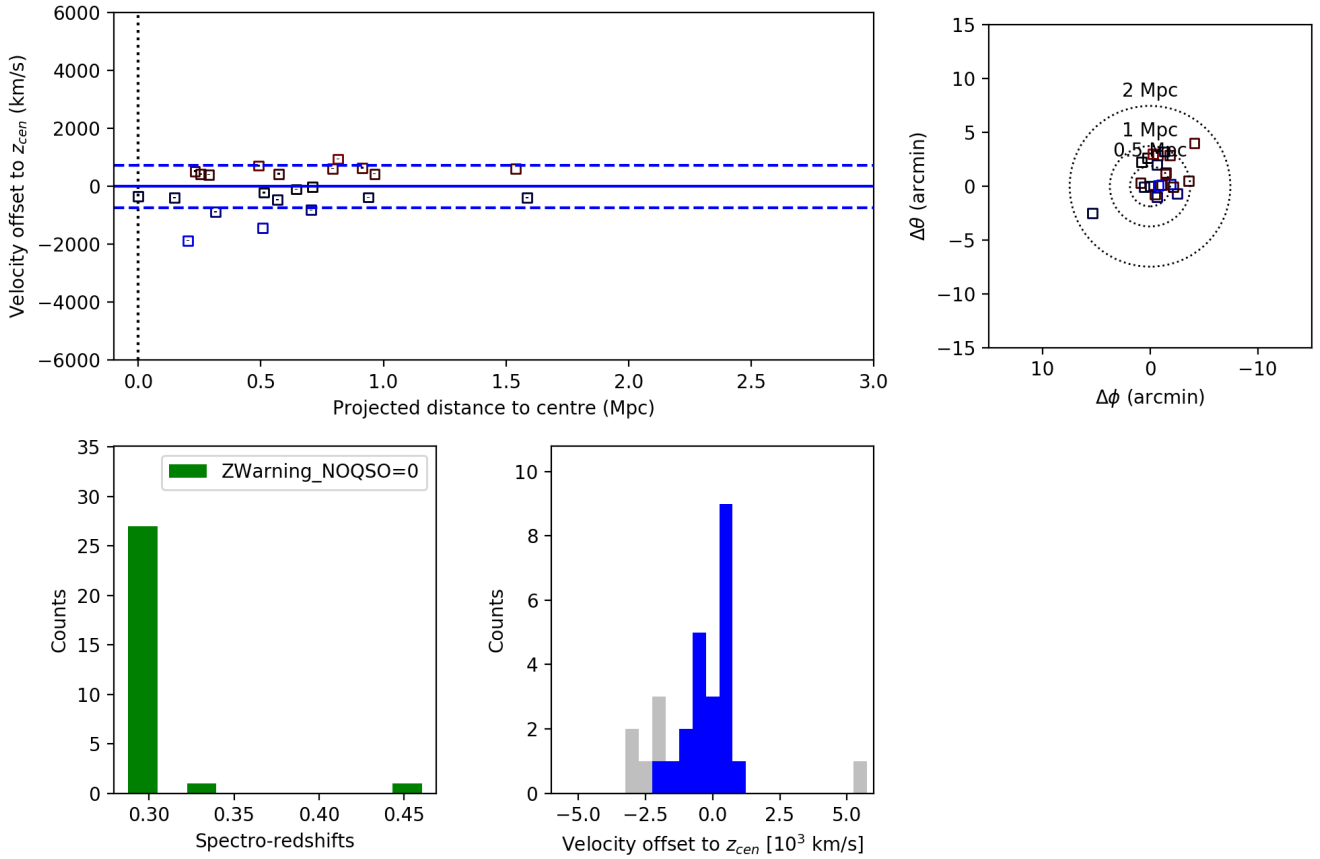


Fig. 5. Spectroscopic redshift validation of a cluster using SPIDERS follow-up observations, as described in Sect. 4.1.3. *Top-left panel:* distribution of red-sequence galaxies in Xclass0842 as a function of their projected distance to the X-ray centroid and the velocity offset to the mean cluster redshift. Blue dashed lines indicate the standard deviation of the velocity distribution. *Top-right panel:* location of those members projected on the sky, with a similar colour-coding as in the previous panel. *Lower-left histogram:* redshift distribution of galaxies in the red sequence with an associated spectroscopic measurement. *Lower-right histogram:* distribution of members (in blue) and non-members (in grey).

clusters and entered the catalogue without any redshift information. The remaining 87 sources retained the ‘provisional’ status, and, though kept in the main public catalogue, are not published online, but are included in Appendix D of the present paper for the interested reader, especially as this list may contain high-redshift cluster candidates.

Misclassified detections are usually due to a point-like source embedded in the extended X-ray emission of a nearby cluster, while high background may also play an important role. The majority of the spurious or misclassified cluster candidates have no visually detected counterpart in the optical band; their X-ray emission was limited within less than $10''$ radius and was usually centred on an optical point source. In addition, we applied machine-learning classification to our provisional sources in order to test the efficiency of such methods in difficult cases. The results are presented in Appendix A.

4.1.3. Spectroscopic follow-up with SPIDERS

A subsample of the previous X-CLASS sample was selected for spectroscopic follow-up within the frame of SPIDERS (SPectroscopic IDentification of eROSITA Sources), a dedicated survey for a homogeneous and complete sample of X-ray active galactic nuclei and galaxy clusters over a large fraction of the sky (Clerc et al. 2016; Dwelly et al. 2017; Salvato et al. 2018; Comparat et al. 2020). The (BOSS) spectrograph mounted on the SDSS-2.5m telescope at Apache Point

Observatory (Gunn et al. 2006) was used. The sample was compiled based on the correlation of X-ray sources from X-CLASS with the RedMapper optical cluster catalogue, as described in Sadibekova et al. (2014) and Clerc et al. (2016). The current catalogue contains 124 validated clusters (out of the 142 targeted) with SPIDERS follow-up spectroscopy up to a redshift of $z \sim 0.6$. The program led to the collection of 1134 spectra in X-CLASS red sequences, with a redshift success rate approaching 99% (Clerc et al. 2020). The median number of galaxies with concordant redshifts used for the redshift validation was ten. Membership is assigned with an algorithm iteratively performing 3σ clipping around the mean redshift. Manual refinements are then allowed in the case of degenerate situations or failures due to the low number of spectroscopic redshifts available. An example cluster is shown in Fig. 5 (see also Kirkpatrick et al. 2021). The list of clusters confirmed with SPIDERS spectroscopy can be found in Table C.1.

4.2. The new X-CLASS catalogue

Following the above classification scheme, the catalogue comprises 1278 X-ray-selected clusters with redshift information: 982 spectroscopically confirmed clusters, 94 with a tentative redshift, and 202 with a photometric redshift. These three categories represent $\sim 78\%$ of the total cluster catalogue and their redshift distribution is presented in Fig. 6. The final catalogue includes an additional 281 clusters with no redshift information. The results

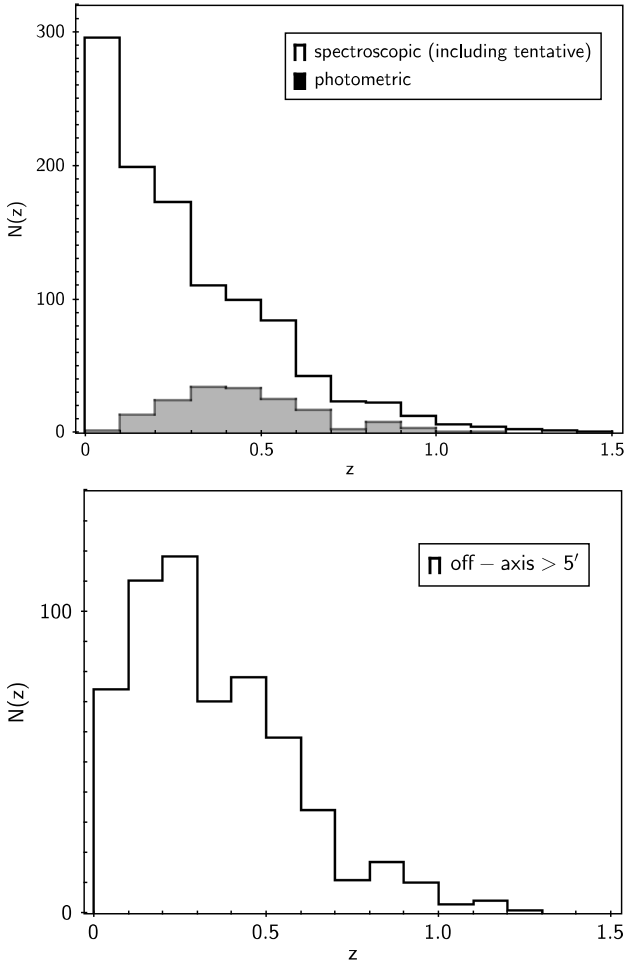


Fig. 6. *Top panel:* redshift distribution of the X-CLASS clusters with available spectroscopic or photometric redshift. *Bottom panel:* redshift distribution for clusters found outside the central $5'$ of the XMM pointings, which excludes pointed observations that bias our sample towards low-redshift values. This distribution peaks around $z_{\text{med}} = 0.29$.

are summarised in Table 2 where they are also split between the two hemispheres, because the availability of observational data is very different. This leads to less confirmed clusters and more with no redshift information in the southern hemisphere.

In addition to the above sources, a small number of detections were flagged as ‘inexistent’ ($\sim 2\%$) and were removed from the catalogue, while the 87 sources that were classified as ‘provisional’ can be found in Table D.1 of the current paper. We caution the interested reader that this list may include a number of spurious or misclassified sources.

Coordinates and redshifts of all cluster galaxies are stored in the cluster database. In the case of confirmed clusters, a histogram with all available spectroscopic redshifts within the corresponding search radius was also produced using the online tool in NED.

4.3. X-ray count-rate measurements

In the database we provide two different X-ray count-rate measurements: the pipeline quantities and a more accurate measurement using a count-rate curve of growth method developed by our team (Clerc et al. 2012).

The pipeline value is the total background-subtracted source count rate in the three *XMM-Newton* detectors

Table 2. Status of the X-CLASS cluster candidates.

Status	Dec > 0	Dec < 0	Total
Confirmed	556	426	982
Tentative	63	31	94
Photometric	51	151	202
No status (no z)	109	172	281
Provisional (no z)	48	39	87
All	827	819	1646

Notes. Sources classified as ‘provisional’ are sources that may not correspond to actual clusters.

(MOS1+MOS2+PN) in the $[0.5-2]$ keV band. This is an automatic measurement provided by the XAmin pipeline fitting procedure (raw pipeline output). It is a measure of the total count rate integrated out to infinity under the assumption that the best-fitting model is correct. The background is locally defined within a box around each source as a flat component that includes both the photon (vignetted) and the particle background, and is fitted simultaneously with the source model parameters. This is a simplified approach because the particle background is in general not flat across the EPIC detectors. Nevertheless, it is justified by the small extent of the vast majority of our sources.

In addition, all sources detected with the XAmin pipeline were subjected to a semi-interactive procedure, described in Sect. 2.4 of CS12, in order to provide more accurate X-ray flux measurements. The sources were assumed to have a circular symmetry to extrapolate measurements on missing parts (masks, CCD gaps, and borders) of the detectors, and to integrate the count rate in concentric annuli. The possibility to interactively alter the segmentation masks was open to the users. The count rate (cts s^{-1}) is the mean number of cluster X-ray photons collected by the three detectors in the direction of the optical axis in one second. The total count rate is the sum of all detector count-rate measurements. A count-rate growth curve as a function of cluster radius is computed from the total count rate. The background was modelled similarly to the respective XAmin automatic procedure. The flat and vignetted background levels were fitted on data extracted in a circular annulus around the source of interest, whose width and position are manually adjusted.

The procedure consists of two steps. The first is an interactive (manual) mode enabling the user to: (a) refine the X-ray cluster centre, (b) remove or correct areas incorrectly masked by XAmin (CCD gaps, unresolved blended sources, FOV edge cases), (c) re-estimate the background level according to the cluster brightness and extension to get a more precise count-rate measurement, (d) optimise the measurements in cases where the source is detected on the missing part of MOS1, and (e) set a more accurate and reliable value for the source radii R_{fit} when the growth curve algorithm has failed because of background overestimation (field source contamination, missing part of MOS1, edge effects). In usual conditions, R_{fit} corresponds to the annulus in which the cluster count-rate uncertainty is compatible with background fluctuations.

The second step is automatically executed when the cluster parameters in the interactive mode have been set. During this step, the count rates are computed in six different bands, namely $[0.5-2]$, $[2-10]$, $[0.5-0.9]$, $[1.3-2]$, $[2-5]$ and $[5-7]$ keV, using a full exposure to obtain the highest signal-to-noise ratio. Settings and measurements for each cluster separately are available in the X-CLASS database on their profile page. An example of the above procedure is illustrated in Fig. 7.

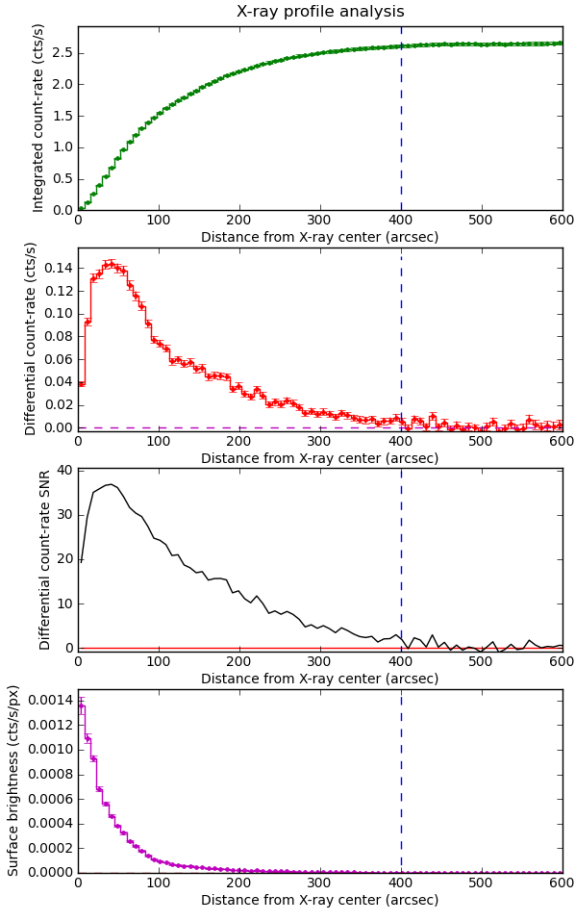


Fig. 7. Interactive background-subtracted count-rate measurement of the X-ray cluster Xclass0047, as described in Sect. 4.3. The blue dashed line in each of the panels indicates the manually defined radius, within which the count-rate measurement is performed.

A comparison between the two kinds of count-rate measurements is shown in Fig. 8 for 1559 clusters for which both measurements are available. For the purpose of this comparison, the count-rate growth curve of each source is evaluated at a fixed angular aperture radius $r = 60''$ and at the source radius $r = R_{\text{fit}}$. On the other hand, the pipeline count-rate measurement is aperture-corrected by means of the best-fit surface brightness model. For sources brighter than $0.1 \text{ counts s}^{-1}$ the agreement between the two measurements is very good: within arcminute-sized apertures, the manually measured count rate is 6% lower on average than the pipeline count rate; it is 4% higher within R_{fit} . At lower count rates, manual measurements enable a more accurate centre positioning, refined background estimates, and more comprehensive source masking, hence recovering most of the failures due to automated model fitting.

4.4. Cluster selection function

In order to model the X-ray-extended selection function of the X-CLASS catalogue, we produced XMM simulations enriched with additional beta-models of a smaller extent, but otherwise identical to those used in CS12. These simulations faithfully reproduce the characteristics of the detectors. We added AGNs following a published $\log N - \log S$ relation (Marconi & Hunt 2003), and unresolved AGNs modelled as a vignettted background component. Unvignettted particle background was also

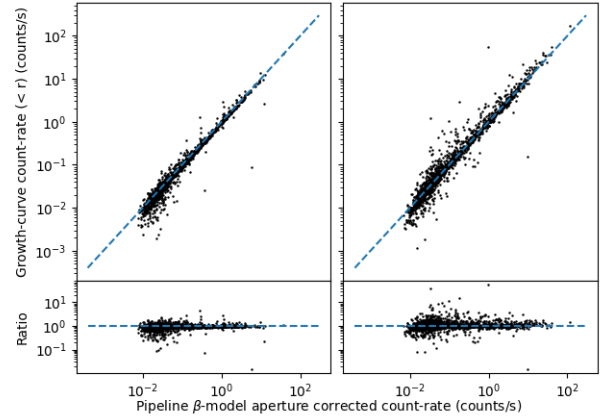


Fig. 8. Comparison between the count rate measured by the source detection pipeline and the manual curve of growth analysis for the 1559 galaxy clusters in the sample. The values represent the equivalent on-axis count rate in the $[0.5-2] \text{ keV}$ energy band combining all three detectors, estimated within identical apertures r . *Left panel:* $r = 1 \text{ arcmin}$. *Right panel:* $r = R_{\text{fit}}$, a radius that is unique to each source and adapted to the signal-to-noise ratio in the measurement images. In both panels, the dashed line represents equality. Uncertainties are only available for manual measurements and are not shown in this figure.

added, parameterised with a factor b . This factor represents the level of enhancement compared to the nominal background level, $b = 1$. Simulations are performed with values of $b = 0.25, 0.5, 1, 2, 4, \text{ and } 8$, and the values of the added particle background as a function of off-axis distance are presented in Fig. 9. Optionally, extended sources as beta-models are distributed at random places on the detector. Their total count rate (in $0.5-2 \text{ keV}$) and apparent core radius are varied while beta is held fixed at $2/3$. The range of count rates spans ($0.0025 \text{ counts s}^{-1} - 0.5 \text{ counts s}^{-1}$). The range of core radii is (3, 5, 10, 20, 50, 100) arcsec.

The number of simulations amounts to 540 for each value of b and for exposure times of 10 and 20 ks. These were all processed with XAmin v3.5 as was briefly described in Sect. 2 to exactly mimic observations. We use a $37.5''$ matching radius for clusters, independently of their extent, flux, and so on, for consistency with previous works (e.g. Pacaud et al. 2006). Sources with multiple associations are ascribed to their nearest neighbour.

In Fig. 10 we present the detection probability of sources within $13'$ off-axis radius from the centre of the observation, for an exposure time of $T_{\text{exp}} = 10 \text{ ks}$ and for background level $b = 1$. It is apparent that the X-CLASS catalogue is not a flux-limited sample, but the selection is rather two-dimensional depending on the extent of the source. Figure 11 illustrates the impact of increasing the background level or the exposure time on the selection of typical X-CLASS clusters (core radii around 20 arcsec). A twofold increase in exposure time provides more numerous low-flux clusters as long as the particle background level remains below three times the fiducial value $b = 1$.

5. The X-CLASS database

The X-CLASS database is built using the MySQL database management system and is accessible to a user through a Java Web Application. The database contains all catalogue meta-data, images and plots, which are available in PNG format generated from pipeline output. The cluster table is dynamically generated using a selection interface and is then displayed as an

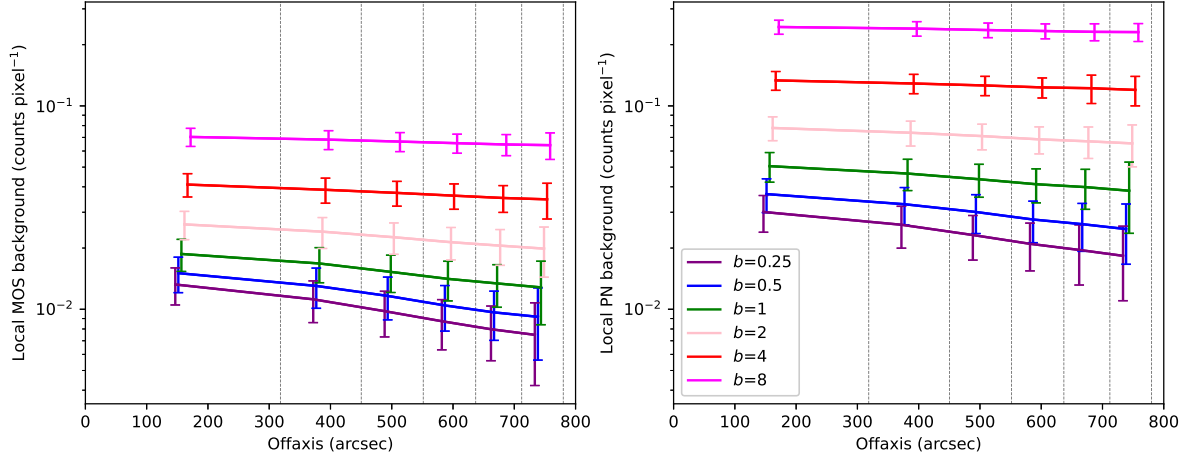


Fig. 9. Calibration of the particle background b parameter as a function of the local background fit by XAmin 3.5 in various equal-area off-axis bins for MOS (*left*) and PN (*right panel*) based on the point-source simulations. Off-axis bin boundaries are represented with vertical dashed lines and data points are slightly shifted on the x -axis for readability. Here, $b = 1$ is the so-called nominal particle background, i.e. close to the most common level encountered in X-CLASS observations. In simulations, particle background is injected at a level of b times the nominal value. The pixel size is $2.5'' \times 2.5''$.

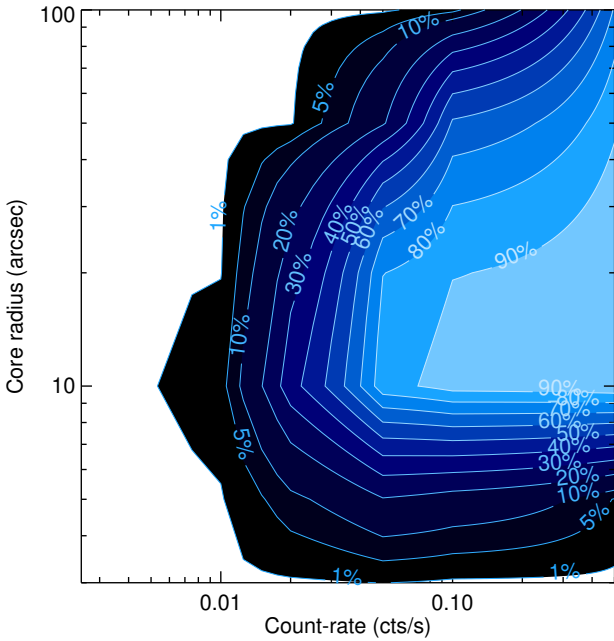


Fig. 10. Contours of the C1 detection probability as a function of total count rate [0.5–2] keV and input core radius of the beta model. Exposure time of $T_{\text{exp}} = 10$ ks and background value of $b = 1$ were used.

HTML web page. Several criteria (redshift, X-CLASS name, X-ray parameters, sky area, etc.) can be applied to refine (constrain) the cluster selection. For each cluster position, there are pre-configured requests to the external astronomical data servers (CDS, NED, NASA/IPAC IRSA) enabled to display optical counterparts and overlays within 3 arcmin. A user manual along with relevant documentation is also available online, as well as the list of X-CLASS publications. The database is hosted in CC-IN2P3 (Centre de Calcul de l'IN2P3 at Lyon in France) and is publicly available online¹.

¹ <https://xmm-xclass.in2p3.fr/>

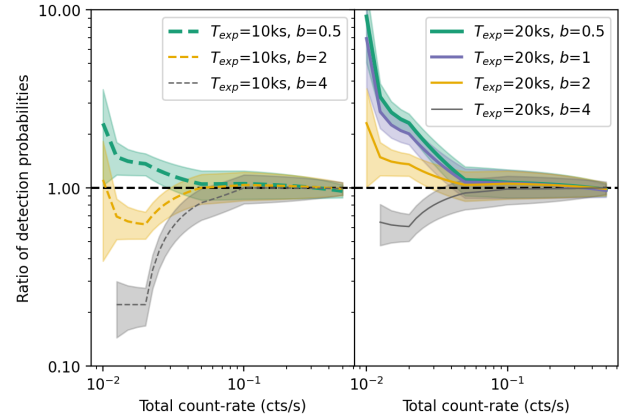


Fig. 11. Variation of the C1 detection efficiency with exposure time and background level. Curves show the ratio relative to the probability shown in Fig. 10 (exposure time of 10 ks and $b = 1$), assuming an apparent core radius $R_c = 20''$. Shaded regions represent the standard deviation around these values, which depends on the number of simulated clusters. Only points with more than nine detected simulated clusters are shown.

The first 20 entries are listed in Table 3, sorted according to increasing RA, while the full version of the catalogue table can be retrieved from the Vizier server at the CDS. From the database graphical interface, the catalogue table provides the following fields for each cluster:

1. *Xclass* – a unique cluster identifier.
2. *RA pipeline* – pipeline-measured right ascension.
3. *Dec pipeline* – pipeline-measured declination.
4. *RA measured* – interactively measured right ascension (see Sect. 4.3).
5. *Dec measured* – interactively measured declination (see Sect. 4.3).
6. *NED* – link to NED data.
7. *obs* – XMM pointing where the cluster is detected.
8. *redshift* – cluster redshift.
9. *status* – redshift validation status (see Sect. 4).

Table 3. X-CLASS cluster database view.

Xclass	RA pipeline	Dec pipeline	RA measured	Dec measured	NED	Obs	Redshift	Status	Total rate	Profile
(1)	(deg.) (2)	(deg.) (3)	(deg.) (4)	(deg.) (5)	(6)	(7)	(8)	(9)	(counts s ⁻¹) (10)	(11)
0020	193.4380	10.1954	193.4380	10.1951	go	0001930301_10ks	0.654	Confirmed	0.049	data
0023	194.2860	-17.4119	194.2920	-17.4064	go	0010420201_10ks	0.047	Confirmed	3.738	data
0033	193.6790	-29.2227	193.6740	-29.2230	go	0030140101_10ks	0.056	Confirmed	5.882	data
0034	193.5950	-29.0162	193.5930	-29.0131	go	0030140101_10ks	0.053	Confirmed	4.362	data
0035	196.2740	-10.2802	196.2740	-10.2787	go	0032141201_10ks	0.34	Photometric	0.047	data
0038	36.5674	-2.6651	36.5677	-2.6663	go	0037981801_10ks	0.056	Confirmed	0.167	data
0039	36.4987	-2.8272	36.4990	-2.8275	go	0037981801_10ks	0.281	Confirmed	0.033	data
0040	35.1871	-3.4339	35.1886	-3.4339	go	0037982601_10ks	0.327	Confirmed	0.050	data
0042	150.1230	-19.6282	150.1220	-19.6292	go	0041180301_10ks		No redshift	0.057	data
0044	202.4460	11.6835	202.4490	11.6848	go	0041180801_10ks	0.204	Confirmed	0.087	data
0047	172.9830	-19.9229	172.9800	-19.9271	go	0042341001_10ks	0.307	Confirmed	3.254	data
0048	173.0280	-19.8611	173.0280	-19.8614	go	0042341001_10ks	0.307	Confirmed	0.154	data
0050	172.8110	-19.9326	172.8130	-19.9343	go	0042341001_10ks	0.46	Photometric	0.025	data
0051	177.6130	1.7580	177.6160	1.7580	go	0044740201_10ks		No redshift	0.036	data
0054	145.9370	16.7402	145.9380	16.7381	go	0046940401_10ks	0.18	Confirmed	0.136	data
0056	145.8820	16.6656	145.8860	16.6671	go	0046940401_10ks	0.255	Confirmed	0.202	data
0057	145.9920	16.6871	145.9950	16.6875	go	0046940401_10ks	0.253	Confirmed	0.057	data
0059	31.9565	2.1553	31.9576	2.1567	go	0052140301_20ks	0.334	Photometric	0.042	data
0062	44.1414	0.1037	44.1417	0.1033	go	0056020301_10ks	0.362	Confirmed	0.778	data
0065	339.2510	-15.2730	339.2520	-15.2731	go	0056021601_10ks	0.31	Photometric	0.316	data
0075	10.4501	-9.4575	10.4507	-9.4569	go	0723802201_20ks	0.056	Confirmed	15.529	data
0078	10.7223	-9.5697	10.7225	-9.5701	go	0065140201_10ks	0.41	Photometric	0.101	data
0079	10.5228	-9.6026	10.5231	-9.6029	go	0065140201_10ks	0.055	Tentative	0.033	data
0082	39.4926	-52.3934	39.4929	-52.3937	go	0067190101_10ks	0.136	Confirmed	0.259	data
0083	148.424	1.6999	148.424	1.6995	go	0070940401_10ks	0.097	Confirmed	0.796	data
0086	348.765	-58.9351	348.766	-58.9354	go	0081340301_10ks	0.44	Photometric	0.034	data
0087	349.094	-59.0752	349.095	-59.0756	go	0081340301_10ks	0.62	Photometric	0.036	data
0088	183.394	2.8953	183.395	2.8963	go	0081340801_10ks	0.410	Confirmed	0.190	data
0095	190.102	-11.8008	190.103	-11.8011	go	0084030101_10ks	0.19	Photometric	0.078	data
0096	9.2778	9.1566	9.2765	9.1583	go	0084230201_20ks	0.252	Confirmed	2.441	data

Notes. (1) X-CLASS unique ID number and link to images and pipeline outputs, (2) right ascension (pipeline automatic measurement), (3) declination (pipeline automatic measurement), (4) right ascension (interactive refined measurement*), (5) declination (interactive refined measurement; for more details see Sect. 4.3), (6) link to NED data. The NED search is within 3', the page is automatically generated using the AladinLite webapp. (7) Observation ID and link to the observation and data processing information page, (8) link to the redshift information page, (9) redshift status, (10) total X-ray count-rate in the [0.5–2 keV] band (pipeline output), (11) link to the interactive X-ray count-rate measurement page. The full table is available at the CDS.

10. *total rate* – pipeline total count-rate.

11. *profile* – link to the interactive X-ray count-rate measurement page.

6. Discussion and comparison with other catalogues

On one hand, the homogeneous selection of the X-CLASS clusters on homogenised observations of 10 and 20 ks exposures simplifies the computation of their selection function and their use in cosmology studies. On the other hand, because of the above selection, the comparison with other similar datasets is difficult (see also relevant discussion in CS12). Nevertheless, within 1' we cross-correlated the X-CLASS catalogue with other X-ray-selected cluster catalogues in order to examine the redshift agreement of the common sources. In Fig. 12 we present such a comparison with two catalogues of X-ray-detected clusters by *XMM-Newton*, XCS (Mehrtens et al. 2012), and 2XMMi/SDSS (Takey et al. 2014), and two by ROSAT, MCXC (Piffaretti et al. 2011) and CODEX (Finoguenov et al.

2020). There is good agreement between redshifts, especially with the MCXC catalogue. We note that in many cases redshifts were obtained from the same source. In cases of large discrepancies we examined our cluster identifications and redshift validation. In most of the discrepant cases, our more recent and updated data allow for a more accurate redshift estimation, while in a limited number of cases, the matched X-ray detections are correlated with different optical counterparts.

We also examined the X-ray luminosity distribution of the matched X-CLASS/XCS cluster sample in order to identify any systematic bias in our selection. In Fig. 13 we plot the distribution of L_{500} [0.05–100] keV, as estimated in Mehrstens et al. (2012) within the R_{500} radius, for both the matched and the full XCS sample. The two samples have very similar luminosity distributions, as also confirmed by a two-sample Kolmogorov–Smirnov test. Therefore, the matched sample is an unbiased subsample of the total XCS sample.

In addition we cross-correlated our catalogue with the 4XMM-DR10 catalogue (Webb et al. 2020). This catalogue includes a large number of extended X-ray sources and their fitting parameters, but does not include any redshift estimation

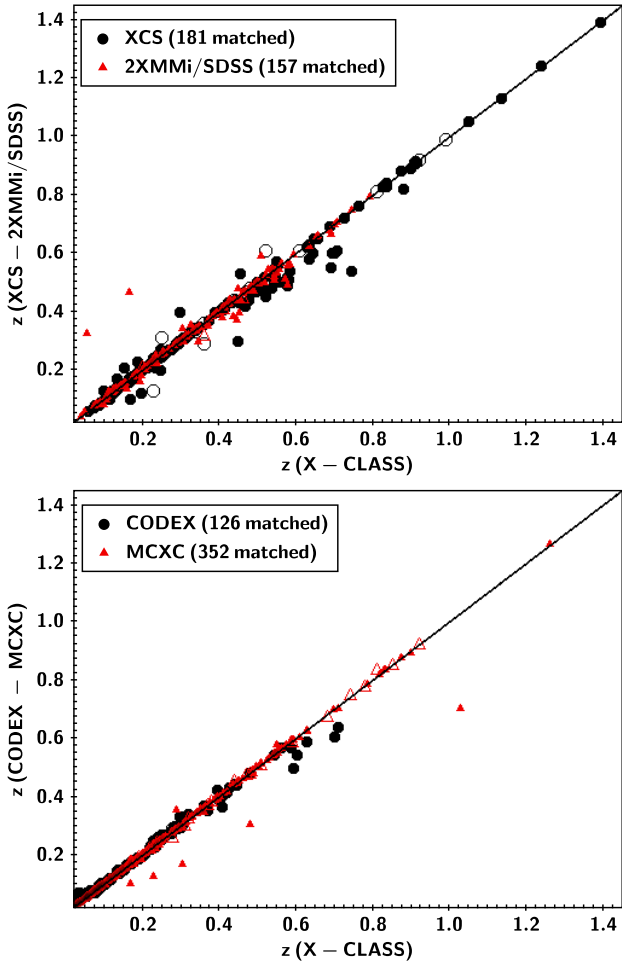


Fig. 12. Redshift comparison between the X-CLASS catalogue and various other X-ray-selected cluster samples. All catalogues include both clusters with spectroscopic and photometric redshifts, except for CODEX, which includes only photometric redshift. The filled (open) shapes mark clusters with spectroscopic (photometric) redshift.

or further examination of their nature. The large majority of the X-CLASS sources are correlated to an extended source in the 4XMM catalogue within $1'$ radius. However, 191 sources are absent, most of which have a provisional status or no redshift information, and inspection of their optical counterpart places them at high redshift. In addition, they usually have a low value for the extent likelihood parameter, as computed by the XAmin pipeline. Nevertheless, a high fraction ($\sim 27\%$) of the uncorrelated clusters have a ‘confirmed’ or ‘photometric’ status, usually below $z = 0.6$.

7. Summary

We present the detection pipeline, selection function, visual inspection, screening, and redshift confirmation of a large number of X-ray-detected galaxy clusters in 4176 archived *XMM-Newton* images. The total number reaches 1646 clusters over 269 deg^2 and the catalogue is publicly accessible via an interactive database constructed and maintained by the X-CLASS Collaboration. The database not only allows the selection of a cluster subsample based on a large variety of criteria, but also gives access to a wealth of meta-data, images, plots, and supplementary information.

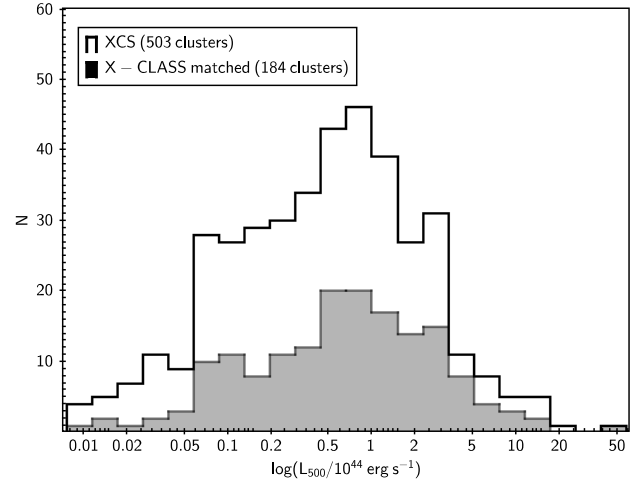


Fig. 13. X-ray bolometric luminosity $L_{500}[0.05-100] \text{ keV}$ distribution of the matched X-CLASS and XCS cluster catalogues. According to a KS two-sample test the null hypothesis that the two samples originate from the same parent distribution cannot be rejected.

The homogeneous selection of the cluster samples over 10 and 20 ks exposures allows the use of the X-CLASS catalogue for cosmological analyses, provided the impact of pointed clusters is accounted for. In addition, the large sky area makes it suitable as a test bed for current and future large-area cluster surveys, such as the ones that will be carried out by the *eROSITA* (Merloni et al. 2012; Predehl et al. 2021), *Athena* (Nandra et al. 2013), and *Euclid* (Laureijs et al. 2011) missions, considering the large amount of human effort and interaction required for the compilation of the present catalogue, which could not be extended to the huge datasets of these missions.

Acknowledgements. The Saclay team acknowledges long term support from the Centre National d’Etudes Spatiales. This research has made use of “Aladin sky atlas” developed at CDS, Strasbourg Observatory, France (Bonnarel et al. 2000; Boch & Fernique 2014). The cross-matching has made use of the NASA/IPAC Extragalactic Database (NED), which is operated by the Jet Propulsion Laboratory, California Institute of Technology, under contract with the National Aeronautics and Space Administration. The Pan-STARRS1 Surveys (PS1) and the PS1 public science archive have been made possible through contributions by the Institute for Astronomy, the University of Hawaii, the Pan-STARRS Project Office, the Max-Planck Society and its participating institutes, the Max Planck Institute for Astronomy, Heidelberg and the Max Planck Institute for Extraterrestrial Physics, Garching, The Johns Hopkins University, Durham University, the University of Edinburgh, the Queen’s University Belfast, the Harvard-Smithsonian Center for Astrophysics, the Las Cumbres Observatory Global Telescope Network Incorporated, the National Central University of Taiwan, the Space Telescope Science Institute, the National Aeronautics and Space Administration under Grant No. NNX08AR22G issued through the Planetary Science Division of the NASA Science Mission Directorate, the National Science Foundation Grant No. AST-1238877, the University of Maryland, Eotvos Lorand University (ELTE), the Los Alamos National Laboratory, and the Gordon and Betty Moore Foundation. Funding for the Sloan Digital Sky Survey IV has been provided by the Alfred P. Sloan Foundation, the US Department of Energy Office of Science, and the Participating Institutions. SDSS acknowledges support and resources from the Center for High-Performance Computing at the University of Utah. The SDSS website is www.sdss.org. SDSS is managed by the Astrophysical Research Consortium for the Participating Institutions of the SDSS Collaboration including the Brazilian Participation Group, the Carnegie Institution for Science, Carnegie Mellon University, Center for Astrophysics/Harvard & Smithsonian (CfA), the Chilean Participation Group, the French Participation Group, Instituto de Astrofísica de Canarias, The Johns Hopkins University, Kavli Institute for the Physics and Mathematics of the Universe (IPMU)/University of Tokyo, the Korean Participation Group, Lawrence Berkeley National Laboratory, Leibniz Institut für Astrophysik Potsdam (AIP), Max-Planck-Institut für Astronomie (MPIA Heidelberg), Max-Planck-Institut für Astrophysik (MPA Garching), Max-Planck-Institut für Extraterrestrische Physik (MPE), National

Astronomical Observatories of China, New Mexico State University, New York University, University of Notre Dame, Observatório Nacional/MCTI, The Ohio State University, Pennsylvania State University, Shanghai Astronomical Observatory, United Kingdom Participation Group, Universidad Nacional Autónoma de México, University of Arizona, University of Colorado Boulder, University of Oxford, University of Portsmouth, University of Utah, University of Virginia, University of Washington, University of Wisconsin, Vanderbilt University, and Yale University. The Legacy Surveys consist of three individual and complementary projects: the Dark Energy Camera Legacy Survey (DECaLS; NSF's OIR Lab Proposal ID 2014B-0404; PIs: David Schlegel and Arjun Dey), the Beijing-Arizona Sky Survey (BASS; NSF's OIR Lab Proposal ID 2015A-0801; PIs: Zhou Xu and Xiaohui Fan), and the Mayall z -band Legacy Survey (MzLS; NSF's OIR Lab Proposal ID 2016A-0453; PI: Arjun Dey). DECaLS, BASS and MzLS together include data obtained, respectively, at the Blanco telescope, Cerro Tololo Inter-American Observatory, The NSF's National Optical-Infrared Astronomy Research Laboratory (NSF's OIR Lab); the Bok telescope, Steward Observatory, University of Arizona; and the Mayall telescope, Kitt Peak National Observatory, NSF's OIR Lab. The Legacy Surveys project is honored to be permitted to conduct astronomical research on Iolkam Du'ag (Kitt Peak), a mountain with particular significance to the Tohono O'odham Nation. The NSF's OIR Lab is operated by the Association of Universities for Research in Astronomy (AURA) under a cooperative agreement with the National Science Foundation. This project used data obtained with the Dark Energy Camera (DECam), which was constructed by the Dark Energy Survey (DES) Collaboration. Funding for the DES Projects has been provided by the US Department of Energy, the US National Science Foundation, the Ministry of Science and Education of Spain, the Science and Technology Facilities Council of the United Kingdom, the Higher Education Funding Council for England, the National Center for Supercomputing Applications at the University of Illinois at Urbana-Champaign, the Kavli Institute of Cosmological Physics at the University of Chicago, Center for Cosmology and Astro-Particle Physics at the Ohio State University, the Mitchell Institute for Fundamental Physics and Astronomy at Texas A&M University, Financiadora de Estudos e Projetos, Fundação Carlos Chagas Filho de Amparo, Financiadora de Estudos e Projetos, Fundação Carlos Chagas Filho de Amparo a Pesquisa do Estado do Rio de Janeiro, Conselho Nacional de Desenvolvimento Científico e Tecnológico and the Ministerio da Ciencia, Tecnologia e Inovacao, the Deutsche Forschungsgemeinschaft and the Collaborating Institutions in the Dark Energy Survey. The Collaborating Institutions are Argonne National Laboratory, the University of California at Santa Cruz, the University of Cambridge, Centro de Investigaciones Energeticas, Medioambientales y Tecnologicas-Madrid, the University of Chicago, University College London, the DES-Brazil Consortium, the University of Edinburgh, the Eidgenössische Technische Hochschule (ETH) Zurich, Fermi National Accelerator Laboratory, the University of Illinois at Urbana-Champaign, the Institut de Ciències de l'Espai (IEEC/CSIC), the Institut de Física d'Altes Energies, Lawrence Berkeley National Laboratory, the Ludwig-Maximilians Universität München and the associated Excellence Cluster Universe, the University of Michigan, the National Optical Astronomy Observatory, the University of Nottingham, the Ohio State University, the University of Pennsylvania, the University of Portsmouth, SLAC National Accelerator Laboratory, Stanford University, the University of Sussex, and Texas A&M University. BASS is a key project of the Telescope Access Program (TAP), which has been funded by the National Astronomical Observatories of China, the Chinese Academy of Sciences (the Strategic Priority Research Program "The Emergence of Cosmological Structures" Grant XDB09000000), and the Special Fund for Astronomy from the Ministry of Finance. The BASS is also supported by the External Cooperation Program of Chinese Academy of Sciences (Grant 114A11KYSB20160057), and Chinese National Natural Science Foundation (Grant 11433005). The Legacy Survey team makes use of data products from the Near-Earth Object Wide-field Infrared Survey Explorer (NEOWISE), which is a project of the Jet Propulsion Laboratory/California Institute of Technology. NEOWISE is funded by the National Aeronautics and Space Administration. The Legacy Surveys imaging of the DESI footprint is supported by the Director, Office of Science, Office of High Energy Physics of the US Department of Energy under Contract No. DE-AC02-05CH1123, by the National Energy Research Scientific Computing Center, a DOE Office of Science User Facility under the same contract; and by the US National Science Foundation, Division of Astronomical Sciences under Contract No. AST-0950945 to NOAO.

References

Adami, C., Giles, P., Koulouridis, E., et al. 2018, *A&A*, **620**, A5
 Andreon, S., Serra, A. L., Moretti, A., & Trinchieri, G. 2016, *A&A*, **585**, A147
 Benson, B. A., de Haan, T., Dudley, J. P., et al. 2013, *ApJ*, **763**, 147

Bertin, E., & Arnouts, S. 1996, *A&AS*, **117**, 393
 Blanton, M. R., Bershad, M. A., Abolfathi, B., et al. 2017, *AJ*, **154**, 28
 Boch, T., & Fernique, P. 2014, *ASP Conf. Ser.*, **485**, 277
 Böhringer, H., Voges, W., Huchra, J. P., et al. 2000, *ApJS*, **129**, 435
 Böhringer, H., Schuecker, P., Guzzo, L., et al. 2001, *A&A*, **369**, 826
 Böhringer, H., Chon, G., & Collins, C. A. 2014, *A&A*, **570**, A31
 Bonnarel, F., Fernique, P., Bienaymé, O., et al. 2000, *A&AS*, **143**, 33
 Cavaliere, A., & Fusco-Femiano, R. 1978, *A&A*, **70**, 677
 Clerc, N., Sadibekova, T., Pierre, M., et al. 2012, *MNRAS*, **423**, 3561
 Clerc, N., Adami, C., Lieu, M., et al. 2014, *MNRAS*, **444**, 2723
 Clerc, N., Merloni, A., Zhang, Y. Y., et al. 2016, *MNRAS*, **463**, 4490
 Clerc, N., Kirkpatrick, C. C., Finoguenov, A., et al. 2020, *MNRAS*, **497**, 3976
 Comparat, J., Merloni, A., Dwelly, T., et al. 2020, *A&A*, **636**, A97
 Dey, A., Schlegel, D. J., Lang, D., et al. 2019, *AJ*, **157**, 168
 Dwelly, T., Salvato, M., Merloni, A., et al. 2017, *MNRAS*, **469**, 1065
 Ebeling, H., Edge, A. C., & Henry, J. P. 2001, *ApJ*, **553**, 668
 Faccioli, L., Pacaud, F., Sauvageot, J. L., et al. 2018, *A&A*, **620**, A9
 Fassbender, R., Böhringer, H., Nastasi, A., et al. 2011, *New J. Phys.*, **13**, 125014
 Finoguenov, A., Guzzo, L., Hasinger, G., et al. 2007, *ApJS*, **172**, 182
 Finoguenov, A., Rykoff, E., Clerc, N., et al. 2020, *A&A*, **638**, A114
 Flewelling, H. A., Magnier, E. A., Chambers, K. C., et al. 2020, *ApJS*, **251**, 7
 Frenk, C. S., White, S. D. M., Efstathiou, G., & Davis, M. 1990, *ApJ*, **351**, 10
 Gioia, I. M., Maccararo, T., Schild, R. E., et al. 1990, *ApJS*, **72**, 567
 Greiner, J., Bornemann, W., Clemens, C., et al. 2008, *PASP*, **120**, 405
 Gunn, J. E., Siegmund, W. A., Mannery, E. J., et al. 2006, *AJ*, **131**, 2332
 Henry, J. P., Gioia, I. M., Maccararo, T., et al. 1992, *ApJ*, **386**, 408
 Henry, J. P., Mullis, C. R., Voges, W., et al. 2006, *ApJS*, **162**, 304
 Kirkpatrick, C. C., Clerc, N., Finoguenov, A., et al. 2021, *MNRAS*, **503**, 5763
 Kosiba, M., Lieu, M., Altieri, B., et al. 2020, *MNRAS*, **496**, 4141
 Laureijs, R., Amiaux, J., Arduini, S., et al. 2011, *ArXiv e-prints* [arXiv:1110.3193]
 Mantz, A., Allen, S. W., Rapetti, D., & Ebeling, H. 2010, *MNRAS*, **406**, 1759
 Mantz, A. B., Abdulla, Z., Allen, S. W., et al. 2018, *A&A*, **620**, A2
 Marconi, A., & Hunt, L. K. 2003, *ApJ*, **589**, L21
 Mehrrens, N., Romer, A. K., Hilton, M., et al. 2012, *MNRAS*, **423**, 1024
 Merloni, A., Predehl, P., Becker, W., et al. 2012, *ArXiv e-prints* [arXiv:1209.3114]
 Nandra, K., Barret, D., Barcons, X., et al. 2013, *ArXiv e-prints* [arXiv:1306.2307]
 O'Sullivan, E., Ponman, T. J., Kolokythas, K., et al. 2017, *MNRAS*, **472**, 1482
 Pacaud, F., Pierre, M., Refregier, A., et al. 2006, *MNRAS*, **372**, 578
 Piccinotti, G., Mushotzky, R. F., Boldt, E. A., et al. 1982, *ApJ*, **253**, 485
 Pierre, M., Valtchanov, I., Altieri, B., et al. 2004, *JCAP*, **9**, 011
 Pierre, M., Chiappetti, L., Pacaud, F., et al. 2007, *MNRAS*, **382**, 279
 Pierre, M., Pacaud, F., Adami, C., et al. 2016, *A&A*, **592**, A1
 Piffaretti, R., Arnaud, M., Pratt, G. W., Pointecouteau, E., & Melin, J. B. 2011, *A&A*, **534**, A109
 Planck Collaboration XX. 2014, *A&A*, **571**, A20
 Plionis, M., López-Cruz, O., & Hughes, D. 2008, *A Pan-Chromatic View of Clusters of Galaxies and the Large-Scale Structure* (Berlin: Springer-Verlag), 740
 Predehl, P., Andritschke, R., Arefiev, V., et al. 2021, *A&A*, **647**, A1
 Ramos-Ceja, M. E., Pacaud, F., Reiprich, T. H., et al. 2019, *A&A*, **626**, A48
 Reblinsky, K., & Bartelmann, M. 1999, *A&A*, **345**, 1
 Ridl, J., Clerc, N., Sadibekova, T., et al. 2017, *MNRAS*, **468**, 662
 Romer, A. K., Viana, P. T. P., Liddle, A. R., & Mann, R. G. 2001, *ApJ*, **547**, 594
 Rozo, E., Wechsler, R. H., Rykoff, E. S., et al. 2010, *ApJ*, **708**, 645
 Rykoff, E. S., Rozo, E., Busha, M. T., et al. 2014, *ApJ*, **785**, 104
 Sadibekova, T., Pierre, M., Clerc, N., et al. 2014, *A&A*, **571**, A87
 Salvato, M., Buchner, J., Budavári, T., et al. 2018, *MNRAS*, **473**, 4937
 Santos, J. S., Fassbender, R., Nastasi, A., et al. 2011, *A&A*, **531**, L15
 Scoville, N., Aussel, H., Brusa, M., et al. 2007, *ApJS*, **172**, 1
 Sehgal, N., Trac, H., Acquaviva, V., et al. 2011, *ApJ*, **732**, 44
 Starck, J. L., & Pierre, M. 1998, *A&AS*, **128**, 397
 Takey, A., Schwöpe, A., & Lamer, G. 2011, *A&A*, **534**, A120
 Takey, A., Schwöpe, A., & Lamer, G. 2013, *A&A*, **558**, A75
 Takey, A., Schwöpe, A., & Lamer, G. 2014, *A&A*, **564**, A54
 Takey, A., Durret, F., Mahmoud, E., & Ali, G. B. 2016, *A&A*, **594**, A32
 van Haarlem, M. P., Frenk, C. S., & White, S. D. M. 1997, *MNRAS*, **287**, 817
 Vikhlinin, A., Burenin, R. A., Ebeling, H., et al. 2009, *ApJ*, **692**, 1033
 Šuhada, R., Song, J., Böhringer, H., et al. 2012, *A&A*, **537**, A39
 Webb, N. A., Coriat, M., Traulsen, I., et al. 2020, *A&A*, **641**, A136
 Willis, J. P., Clerc, N., Bremer, M. N., et al. 2013, *MNRAS*, **430**, 134
 Wright, E. L., Eisenhardt, P. R. M., Mainzer, A. K., et al. 2010, *AJ*, **140**, 1868

Appendix A: Convolutional neural network classification of the provisional sources

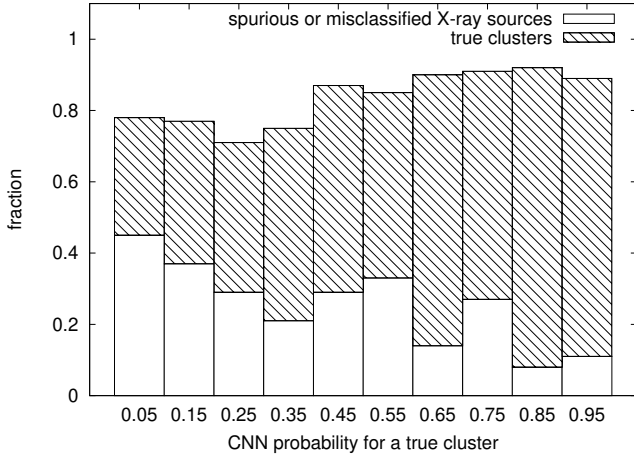


Fig. A.1. Agreement between CNN classification and expert opinion. The hatched area shows the fraction of sources agreed upon by all researchers as being true clusters, while the empty area shows the false detections agreed upon by all researchers. The percentage of sources for which the expert opinions are mixed is omitted for clarity, but these sources account for the remaining fraction up to 1 for each bin. The number of sources in each bin varies from 10 to 33. CNNs are shown to be more effective in identifying true clusters in the last two bins (CNN prob. $> 80\%$) and false detections in the first bin (CNN prob. $< 10\%$).

Convolutional neural networks (CNNs) are state-of-the-art machine-learning tools for image classification. In [Kosiba et al. \(2020\)](#), our team developed a custom CNN architecture for automatic classification of galaxy cluster candidates into two classes, ‘galaxy cluster’ and ‘non-cluster’. To train the network, we provided it with X-ray and optical images of approximately 1500 galaxy cluster candidates together with their manual classifications as given by experts from the X-CLASS Collaboration. The network used those data to learn how to understand patterns of different classes of objects and projection and instrumental effects of the data. When successfully trained, we evaluated the performance of the network on a sample of 85 spectroscopically confirmed galaxy clusters and 85 objects we classified as non-clusters. Our network achieved $\sim 90\%$ accuracy. For more technical details on the construction of the data and our CNN architecture, we kindly refer the interested reader to [Kosiba et al. \(2020\)](#).

Here, we compare the CNN classifications with the expert opinions on the 225 ‘provisional’ sources as described in Sect. 4.1.2. The results are illustrated in Fig. A.1. Mixed expert opinions are not included in the histogram but they can easily be inferred as the remaining percentage in each bin. We clearly see that the CNN method is most successful in classifying sources as clusters with more than 80% probability (the last two bins). The agreement in both these bins is $\sim 80\%$. We conclude that, as expected, automatic classification of X-ray sources is more efficient at identifying true bonafide clusters than at discarding spurious or misclassified ones.

We stress that the CNN was not trained on provisional sources because these could not be labelled as ‘galaxy clusters’ or ‘non-clusters’ by definition of this class. The provisional sources are galaxy cluster candidates that the experts were not sure how to classify in the first manual screening, making them the hardest-to-classify galaxy cluster candidates.

However, further training of our CNN on a large sample of difficult cases with known true classification (e.g. spectroscopic confirmation) would make it more reliable for classification of difficult provisional sources and especially useful for large-area surveys where human interaction will be impossible.

Appendix B: Detected sources on observed fields with less than three detectors

Table B.1. X-ray clusters detected on *XMM-Newton* observations with less than three detectors.

RA (deg.)	Dec (deg.)	Redshift	Status	Available detectors
7.436	4.873	0.206	Confirmed	MOS1+MOS2
8.664	-12.12	0.44	Photometric	MOS1+MOS2
110.22	71.151	0.231	Confirmed	MOS1+MOS2
131.797	34.813	0.552	Confirmed	MOS1+MOS2
154.798	45.047	–	–	MOS1+MOS2
155.151	45.005	–	Provisional	MOS1+MOS2
175.353	-12.279	0.115	Tentative	MOS1+MOS2
226.499	1.697	0.237	Tentative	PN
156.059	4.193	–	Provisional	PN

Notes. Redshift and status as defined in Sect. 5.

In this section, we provide a table of the additional nine X-ray extended sources that were detected on observations with one or two missing detectors.

Appendix C: X-CLASS clusters spectroscopically confirmed with SPIDERS

In Table C.1 we present the subsample of 124 clusters selected for spectroscopic follow-up within the frame of SPIDERS (see Sect. 4.1.3).

Table C.1. X-CLASS clusters spectroscopically confirmed with SPIDERS (see Sect. 4.1.3).

Xclass	N_z	Obs. status	N_{mem}	Zspec	Xclass	N_z	Obs. status	N_{mem}	Zspec
0039	12	Complete	7	0.2810 ± 0.0009	1624	15	Complete	12	0.2276 ± 0.0009
0040	15	Complete	12	0.3274 ± 0.0009	1626	5	Complete	5	0.548 ± 0.002
0062	18	Complete	18	0.362 ± 0.002	1627	16	Complete	15	0.3297 ± 0.0009
0096	17	Complete	16	0.252 ± 0.001	1635	11	Complete	8	0.428 ± 0.001
0099	26	Complete	22	0.2311 ± 0.0007	1637	24	Complete	22	0.206 ± 0.001
0102	15	Complete	14	0.0593 ± 0.0003	1642	14	Complete	9	0.55 ± 0.01
0103	12	Complete	11	0.1320 ± 0.0005	1674	17	Complete	8	0.580 ± 0.001
0108	19	Complete	14	0.1949 ± 0.0006	1676	27	Complete	14	0.2881 ± 0.0004
0109	12	Complete	9	0.478 ± 0.001	1678	24	Complete	18	0.409 ± 0.002
0110	24	Complete	14	0.2703 ± 0.0009	1680	4	Complete	3	0.552 ± 0.004
0169	10	Complete	9	0.320 ± 0.002	1686	11	Complete	6	0.3076 ± 0.0009
0224	15	Complete	11	0.1423 ± 0.0006	1706	9	Incomplete	6	0.3321 ± 0.0004
0245	10	Complete	7	0.1603 ± 0.0003	1737	21	Complete	20	0.276 ± 0.001
0270	15	Complete	12	0.2452 ± 0.0006	1738	20	Complete	18	0.280 ± 0.002
0336	17	Complete	13	0.421 ± 0.001	1758	7	Complete	6	0.342 ± 0.001
0342	4	Incomplete	3	0.230 ± 0.003	1763	9	Complete	4	0.3124 ± 0.0006
0343	17	Incomplete	15	0.351 ± 0.001	1764	15	Complete	8	0.311 ± 0.001
0344	14	Complete	11	0.2909 ± 0.0006	1789	10	Complete	2	$0.59^{(1)}$
0347	3	Incomplete	2	$0.26^{(1)}$	1807	16	Complete	10	0.4999 ± 0.0006
0349	28	Complete	22	0.1537 ± 0.0005	1816	10	Complete	3	0.579 ± 0.001
0361	8	Complete	7	0.0454 ± 0.0007	1817	9	Complete	5	0.579 ± 0.002
0377	9	Incomplete	8	0.395 ± 0.002	1853	33	Complete	26	0.2972 ± 0.0008
0574	8	Complete	4	0.497 ± 0.002	1854	14	Complete	8	0.519 ± 0.001
0578	30	Complete	29	0.1396 ± 0.0007	1855	11	Complete	8	0.1865 ± 0.0007
0615	11	Complete	6	0.255 ± 0.001	1866	2	Complete	2	$0.44^{(1)}$
0628	7	Complete	6	0.2323 ± 0.0006	1900	13	Complete	8	0.413 ± 0.002
0630	5	Complete	4	0.373 ± 0.001	1904	34	Complete	32	0.0895 ± 0.0003
0632	19	Complete	14	0.3947 ± 0.0005	1941	17	Complete	14	0.0996 ± 0.0003
0638	6	Complete	4	0.500 ± 0.001	1957	23	Complete	23	0.2696 ± 0.0009
0686	8	Complete	4	0.460 ± 0.003	1982	10	Complete	6	0.248 ± 0.001
0706	5	Complete	4	0.609 ± 0.002	1983	10	Complete	9	0.3453 ± 0.0004
0734	6	Complete	4	0.427 ± 0.004	2003	7	Complete	5	0.532 ± 0.003
0740	14	Complete	9	0.3388 ± 0.0008	2026	8	Complete	4	0.527 ± 0.001
0755	18	Complete	14	0.1969 ± 0.0004	2034	6	Incomplete	5	0.248 ± 0.001
0841	13	Complete	7	0.551 ± 0.003	2036	13	Complete	6	0.328 ± 0.001
0842	29	Complete	22	0.3009 ± 0.0009	2051	17	Complete	9	0.411 ± 0.002
0890	19	Complete	13	0.3397 ± 0.0007	2080	11	Complete	6	0.427 ± 0.002
0908	16	Complete	11	0.2744 ± 0.0005	2081	21	Complete	19	0.293 ± 0.002
0953	12	Complete	7	0.1327 ± 0.0002	2088	13	Complete	11	0.0900 ± 0.0009
0963	13	Complete	12	0.2477 ± 0.0005	2090	26	Complete	25	0.0904 ± 0.0006
1013	10	Complete	8	0.4149 ± 0.0005	2093	21	Complete	16	0.2970 ± 0.0008
1059	26	Complete	22	0.2791 ± 0.0005	2097	19	Complete	18	0.1125 ± 0.0006
1062	26	Complete	22	0.1238 ± 0.0004	2109	25	Complete	20	0.2128 ± 0.0006
1069	9	Complete	9	0.1328 ± 0.0004	2154	8	Complete	7	0.329 ± 0.001
1086	7	Complete	7	0.423 ± 0.002	2155	9	Complete	8	0.390 ± 0.001
1159	22	Complete	20	0.412 ± 0.001	2182	6	Complete	6	0.520 ± 0.002
1185	11	Complete	5	0.492 ± 0.002	2208	13	Complete	8	0.1050 ± 0.0004
1288	18	Complete	13	0.532 ± 0.002	2214	20	Complete	15	0.3004 ± 0.0004
1307	28	Complete	26	0.0593 ± 0.0004	2272	13	Complete	9	0.254 ± 0.003
1350	4	Incomplete	3	0.396 ± 0.001	2295	28	Complete	22	0.3695 ± 0.0007
1351	11	Incomplete	6	0.543 ± 0.002	2328	2	Complete	2	$0.45^{(1)}$
1368	23	Complete	20	0.288 ± 0.001	2338	31	Complete	29	0.1406 ± 0.0004
1369	12	Complete	5	0.284 ± 0.002	2340	12	Complete	11	0.443 ± 0.002
1386	13	Complete	12	0.314 ± 0.001	2344	21	Complete	21	0.232 ± 0.002
1439	23	Complete	21	0.0573 ± 0.0006	2345	22	Complete	20	0.219 ± 0.001
1443	31	Complete	24	0.0543 ± 0.0006	2347	28	Complete	26	0.1672 ± 0.0007
1451	8	Complete	6	0.478 ± 0.004	2348	26	Complete	25	0.1921 ± 0.0009
1452	7	Complete	5	0.447 ± 0.004	2350	23	Complete	20	0.412 ± 0.001
1543	10	Complete	10	0.370 ± 0.001	2353	25	Complete	23	0.190 ± 0.001
1544	19	Complete	18	0.370 ± 0.001	2358	30	Complete	25	0.0949 ± 0.0007
1548	5	Complete	5	0.3281 ± 0.0006	2360	14	Complete	10	0.235 ± 0.002
1622	21	Complete	14	0.0794 ± 0.0003	2363	14	Complete	8	0.312 ± 0.002

Notes. This table lists the systems that are validated with N_{mem} spectroscopic redshifts selected among N_z redshifts available in their red sequence. The observational status indicates ‘complete’ if all selected targets led to a spectrum acquisition. The spectroscopic redshift uncertainty reflects the spread in the N_{mem} redshift values. A few systems marked with (1) were confirmed with only two spectroscopic members, hence no uncertainty is given on the redshift.

Appendix D: Provisional sources

Table D.1 presents the subsample of 87 candidate clusters for which the visual screening (see Sect. 4.1.2) did not provide a

conclusive result. These sources are not included in the online public catalogue.

Table D.1. X-CLASS clusters classified as ‘provisional’.

Xclass	RA (deg.)	Dec (deg.)	Total rate (counts s ⁻¹)	Xclass	RA (deg.)	Dec (deg.)	Total rate (counts s ⁻¹)
20070	0.792	-29.968	0.05688	3424	169.214	17.987	0.03811
0489	11.785	25.278	3.66885	1894	169.572	7.971	0.01281
0486	11.858	-25.126	0.03257	0231	172.902	-34.695	0.02231
0508	16.507	-80.151	0.03299	2268	178.981	23.403	0.01315
0889	20.281	3.826	0.01776	22889	180.352	-18.832	0.01657
3146	23.316	30.746	0.04004	21578	184.771	5.819	0.02551
20173	32.009	35.463	0.02230	23494	186.144	7.186	0.01566
20828	32.556	-0.198	0.03283	3390	186.307	12.662	0.12703
1850	34.570	-73.938	0.03450	21781	188.338	70.765	0.04260
21766	34.963	-6.148	0.01781	0497	188.965	12.498	0.01774
3378	37.592	-60.554	0.15114	2105	194.340	26.898	0.01816
3020	40.277	-8.315	0.01193	2103	194.450	27.402	0.04238
3334	40.876	32.421	0.30850	0560	195.646	-2.307	0.02117
3093	50.413	-37.128	0.03664	21170	197.706	57.658	0.05172
2426	50.602	-37.160	0.08201	23576	198.539	-16.381	0.03641
20052	54.544	0.318	0.03535	0447	201.280	-38.507	0.34308
3398	55.118	-18.574	0.02939	1359	202.274	58.447	0.02694
1709	56.078	24.589	0.01932	20318	203.157	-31.798	0.07504
22693	58.565	-59.036	0.01911	20177	204.294	51.931	0.03124
20953	61.904	-12.364	0.03154	0406	209.029	18.395	0.06527
2502	62.600	-75.231	0.02606	0071	211.053	-33.858	0.05082
1981	63.084	-28.533	0.01731	3368	211.633	25.134	0.00993
2343	68.093	-13.263	0.03117	3369	211.732	25.011	0.01606
1292	72.174	-66.052	0.04434	3113	213.205	-34.298	0.02489
3116	73.702	-10.254	0.02499	1766	213.722	36.205	0.08474
2288	83.290	-62.426	0.01029	20700	222.450	8.906	0.03159
23586	86.227	-25.738	0.01752	2372	227.778	70.718	0.04958
21432	117.482	55.862	0.03641	0907	233.187	32.712	0.01681
1930	122.110	-76.477	0.01407	22703	251.264	57.630	0.03171
3305	122.209	20.932	0.02117	3193	251.927	34.955	0.06984
3457	139.828	-11.985	0.01521	24820	260.420	57.876	0.02510
1618	144.532	71.116	0.01495	3165	262.827	6.031	0.01854
3085	145.470	46.854	0.02163	0204	314.015	-4.524	0.01769
1679	145.594	46.982	0.01284	1823	322.931	-42.876	0.02355
1777	146.697	9.805	0.26240	24447	324.265	-63.133	0.03605
21197	149.694	2.264	0.03038	21444	330.691	18.841	0.02231
2316	152.129	12.202	0.01674	2844	333.578	-10.265	0.03685
0434	156.059	4.192	0.00467	21706	334.159	-36.817	0.03245
24309	161.450	4.364	0.08199	22786	339.026	34.182	0.02820
23209	162.955	57.546	0.01016	2052	344.267	-43.337	0.03379
22477	163.180	10.547	0.01799	2159	349.022	-2.428	0.04161
0813	163.192	57.355	0.01775	1911	349.555	-42.193	0.05136
22475	163.281	10.707	0.03708	21587	352.266	14.865	0.04891
3060	164.630	1.634	0.02172				